UCRL-19709

c.2

WEAK INTERACTIONS: ON THE EXISTENCE OF NEUTRAL LEPTONIC CURRENTS

Rolland P. Johnson
(Ph.D. Thesis)

April 2, 1970

AEC Contract No. W-7405-eng-48

LAWRENCE RADIATION LABORATORY
UNIVERSITY of CALIFORNIA BERKELEY

UCRL-19709

DISCLAIMER

WEAK INTERACTIONS: ON THE EXISTENCE OF NEUTRAL LEPTONIC CURRENTS

Contents

UCRL-19709

WEAK INTERACTIONS: ON THE EXISTENCE OF NEUTRAL LEPTONIC CURRENTS

Rolland P. Johnson

Lawrence Radiation Laboratory
University of California
Berkeley, California

March 20, 1970

ABSTRACT

New upper limits to the branching ratios for $K_L^o \to \mu^+ \mu^-$, $K_L^o \to e^+ e^-$, and $K_L^o \to \mu^\pm e^\mp$ have been set. A two-armed spectrometer system for the simultaneous detection of these decay modes and the normalizing $K_L^o \to \pi^+ \pi^-$ mode is described. No events of the $\mu\mu$, ee or μe type were observed. Twenty-three thousand $K_L^o \to \pi^+ \pi^-$ events with detection efficiency corrections then determine new branching ratio upper limits relative to all K_L^o modes of 1.1×10^{-7} (90% C.L.) for all three leptonic modes.

I. INTRODUCTION

This paper describes a Bevatron experiment to search for three rare decay modes of the long-lived neutral K meson. The third chapter describes the double-spectrometer system used in the experiment in some detail and may be bypassed by the reader if the general discussion in Chapter II is found to be sufficient.

A. Theoretical Interest in $K_L^o \rightarrow \mu^+\mu^-$, $\mu^\pm e^\mp$, e^+e^-

It is known that the present-day picture of weak interactions is wrong at least to the extent that it is incomplete. For example, the accepted methods applied to neutrino-electron scattering imply an impossibly large cross-section for neutrino energies above a few hundred GeV.[1] On the other hand many convincing calculations can be made which show our knowledge of the low energy aspects of weak interactions to be considerable, especially when strong interactions can be eliminated.

The impossible results of the neutrino-electron cross-section calculation indicate something conceptual is missing. Indeed, one of the major interests in very high energy accelerators is the possibility of neutrino beams of high enough energy and intensity to allow the comparison of predicted and actual cross-sections. The hope is that the differences will give some hint to guide the theory of weak interactions. In the experiment described here, rare decay modes of the neutral K meson were examined in the hope that very precise measurements might give some hints for further theoretical development.

Neutral K decays into pairs of charged leptons have never been observed. There are no compelling arguments as to whether such purely weak decays should or should not exist.

The three following sections describe in more detail some aspects of theory to which the leptonic, neutral kaon decays are relevant.

1. Effective Lagrangian

In the contemporary picture of the weak current–current interaction, the currents are composed of a sum of terms each necessary to describe known weak phenomena. The leptonic part has two terms.[2]

$$j_\alpha \text{ (leptonic)} = \bar{u}_e \gamma_\alpha (1 + \gamma_5) u_{\nu_e} + \bar{u}_\mu \gamma_\alpha (1 + \gamma_5) u_{\nu_\mu},$$

where the u's are 4–component free particle solutions to the Dirac equation, and the γ's are the 4 x 4 Dirac matrices.

All known weak interactions involving leptons can be calculated using this current and its conjugate. Some not yet observed (such as the previously mentioned neutrino–electron interaction) can be calculated with this expression.

Notice that in the expression for the leptonic current the electron and the electron neutrino are associated with each other as are the muon and the muon neutrino. These pairs have a net non–zero electric charge and this defines the leptonic part as a charged current. The 2–lepton decay modes of the K_2^o, if they occur in first order in the weak interaction Lagrangian, are necessarily due to a neutral current.

The existence of the particular decay modes searched for here might imply the existence of neutral components of the current such as

$$\bar{u}_e \gamma_\alpha (1 + \gamma_5) u_e, \bar{u}_\mu \gamma_\alpha (1 + \gamma_5) u_\mu \text{ or } \bar{u}_\mu \gamma_\alpha (1 + \gamma_5) u_e.$$

These elements would have to be suppressed in the expression for the weak current if they do exist, for they have obviously not been detected on a level comparable to the charged leptonic current. It is not impossible, however, to imagine the occurrence of a natural suppression factor analogous to the Cabbibo angle[3] which describes the relative strengths of the strangeness-changing and non-strangeness changing weak interactions.

In the framework of the vector-axialvector (V-A) form for the currents the relative rates for $K_L^o \rightarrow \mu\mu$, μe, ee are easily calculated to be approximately 40 000: 20 000: 1. (See Appendix A.) If the V-A form degenerates to scalar-pseudoscalar the relative rates become about equal.

2. Higher Order Weak Interactions

Another possibility is that the two leptonic decay modes of the K_L^o represent the occurrence of 2nd or higher order weak interactions.[4] One way of getting the 2 lepton modes in 2nd order is with an intermediate boson, i.e.

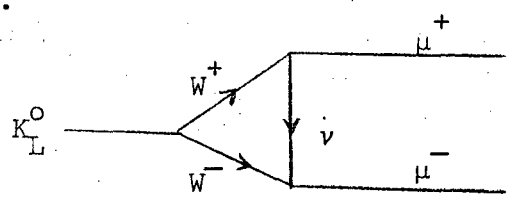

In fact Ioffe and Shabalin[5] have calculated the branching ratio for this mode using current algebra and standard Feynman techniques. The divergent integral which one gets in integrating around the $WW\nu$ loop gives an infinite

answer unless one invokes a cut-off. Ioffe and Shabalin argue that one obtains a natural cut-off due to the mass of the boson. Thus by measuring the rate of $K_L^o \to \mu\mu$ or setting an upper limit to the branching ratio one can set an upper limit to the mass of the W. This and the W production experiments which have set lower limits to the mass may eventually prove that the intermediate boson does not exist!

3. Electromagnetic Effects

One reason that the $K_L^o \to \ell\ell$ is a good place to look for small weak effects is that the electromagnetic effects are small and somewhat amenable to calculation. The $K_L^o \to$ 2 photon branching ratio has been measured[6] to be about 4.5×10^{-4}. Assuming the $K\gamma\gamma$ vertex to be the same as the measured value and using standard quantum electrodynamics on the diagram below gives a lower limit of about 4.5×10^{-9} for the $K_L^o \to \mu^+ \mu^-$ branching ratio.[7]

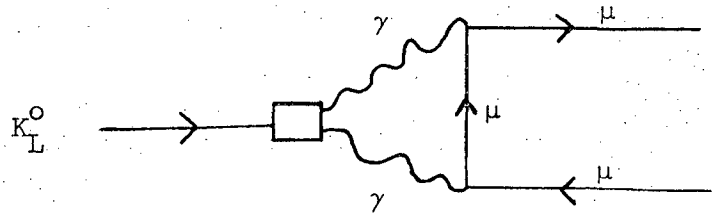

The catch and the physics in this process is that the photons may be virtual photons in the K_L^o decay and this can cause the branching ratio to be somewhat enhanced. The Feynman diagram can be evaluated but the $\gamma\gamma\mu$ loop gives a logarithmic divergence just as Ioffe and Shabalin's $WW\nu$ loop did. And in the same way one has to invoke a cut-off. Quigg and Jackson[7] have used a vector dominance model and integrated to the mass of the Φ to get an enhancement factor of ~ 1.4. Other calculations using similar techniques seem to give the same enhancement factor.[8]

It might be noted that the same calculation for $\eta^o \rightarrow \mu\mu$ has been made by Quigg and Jackson.[7]

The results of an experiment to measure this mode[9] seem to indicate the rate is higher than anticipated by a factor of 4. If the $K \rightarrow \mu\mu$ rate is also anomolously large by a similar factor it could be because the divergent loop evaluation (common to both predictions) is incorrect.

Electromagnetic contributions to the $K_L^o \rightarrow \mu^+ e^{\mp}$ rate are not expected due to the conservation of lepton number in electromagnetic interactions. The $K_L^o \rightarrow e^+ e^-$ mode compared to the $K_L^o \rightarrow \mu^+\mu^-$ mode is suppressed by a factor of $(m_e/m_\mu)^2 \approx 1/40\ 000$. This result of quantum electrodynamics is the same as for a purely weak decay involving neutral currents. (See Appendix A.)

B. Past Measurements Relevant to This Work

Table I on page 6 contains results of previous measurements of the rare decay modes of the K_L^o. Only the most recent or most precise are included. Also in the table are results of other searches for neutral leptonic currents.

Finally, specific decays mentioned in the introduction are included.

TABLE I

Decay Mode	Branching Ratio to All Modes (limits are 90% C.L.)	Reference[10]
Leptonic Modes of K_L^o		
$K_L^o \to \mu^+ \mu^-$	$< 2.1 \times 10^{-7}$	Foeth
	$(< 2.1 \times 10^{-8})$	Rubbia
	$< 1.6 \times 10^{-6}$	Bott–Bodenhausen
$K_L^o \to \mu^\pm e^\mp$	$< 8 \times 10^{-6}$	Fitch
	$< 9 \times 10^{-6}$	Bott–Bodenhausen
$K_L^o \to e^+ e^-$	$< 1.5 \times 10^{-7}$	Foeth
	$< 1.8 \times 10^{-5}$	Bott–Bodenhausen
Other Neutral Leptonic Currents		
$K_S^o \to \mu^+ \mu^-$	$< 7.3 \times 10^{-5}$	Bott–Bodenhausen
$K^+ \to \pi^+ \mu^+ \mu^-$	$< 3 \times 10^{-6}$	Camerini 1
$K^+ \to \pi^+ e^+ e^-$	$< 1.1 \times 10^{-6}$	Camerini 2
$K^+ \to \pi^+ \nu \bar{\nu}$	$(< 7.7 \times 10^{-7})$	Stiening
$K^+ \to \pi^+ \pi^o e^+ e^-$	$< 8 \times 10^{-6}$	Cline
$\mu^+ \to e^+ \gamma$	$< 2.2 \times 10^{-8}$	Parker
$\mu^+ \to e^+ e^- e^+$	$< 1.8 \times 10^{-7}$	Alikhanov
Other Measurements		
$K_L^o \to \gamma \gamma$	$4.68 \pm 0.64 \times 10^{-4}$	Banner
$\eta^o \to \gamma \gamma$	$.381 \pm .023$	Data Group
$\frac{\Gamma(\eta^o \to \mu^+ \mu^-)}{\Gamma(\eta^o \to \gamma \gamma)}$	$5.9 \pm 2.2 \times 10^{-5}$	Hyams[9]
	$< 2 \times 10^{-5}$	Wehmann

II. EXPERIMENTAL METHOD

A. Overall Description of Technique

The 2 lepton decay modes of the K_L^o are distinguished from the more common modes by having higher center of mass momenta (p^*). See p.49, Table II. One can exploit this characteristic by accepting those events decaying so that the momentum transverse to a K_L^o beam is above a minimum value. Ignoring complications of beam divergence and center of mass solid angle for the moment, a spark chamber trigger scheme can be easily described.

The relationship between momentum p and radius of curvature ρ for a charged particle moving in a magnetic field is

$$p\ (\mathrm{MeV/c}) = 30\ B_\perp \rho\ (\text{kilogauss-Meters}) \qquad (1)$$

Magnets of the type used in this experiment can generally be characterized by a constant effective length,

$$\ell = \rho\ 2\ \sin\frac{\theta}{2} \approx \rho\ \sin\theta \qquad (2)$$

where ρ is the same as above and θ is the bending angle. See Fig. 1.

Consider a K_L^o passing by a region of field described by (2). Let it decay such that the secondary is emitted nearly perpendicular to the kaon's direction in the kaon's center of mass (i.e., $\cos\theta^* \approx 0$. See Fig. 2.)

Combining (1) and (2)

$$p\ \sin\theta = 30\ B_\perp \ell$$

where $B_\perp \ell$ is a constant, the line integral of the magnet. But $p\ \sin\theta = p^*$

is not affected by a Lorentz transformation and the secondary will be bent parallel to the beam line independent of the primary momemtum. With a magnet of constant line integral chosen to be equal to $p^*/30$ any secondary with transverse momentum p^* will be bent parallel to the direction of the primary particle.

Decay modes other than the dileptonic generally have smaller transverse momenta and are deflected more toward the beam line.

In this experiment scintillation counters arranged behind the magnets sensed particles with trajectories approximately parallel to the beam line, and triggered spark chambers to record the event for later kinematic analysis. Figure 3 shows the spatial relationships of the beam, magnets, and scintillation counters.

Shown also in Fig. 3 are the Cherenkov counters and range determination system. Electrons were detected in the threshold Cherenkov counters filled with Freon 12 and pions were distinguished from muons by having shorter range in the carbon, iron and scintillator range detectors.

B. Critical Points of the Experimental Method

The identification of the double leptonic decay modes to the exclusion of background events can be made certain if the constraints are strong enough. The momentum and position have to be measured extremely well for each secondary particle and the identity of the particle has to be known with certainty.

Knowing the momenta and directions of the two secondaries before the magnets, one can test for a common intersection point, a vertex, and trace the primary particle's path back to the target. Requiring

the origin of the event to be the target is the same as requiring the decay to be coplanar and consistent with momentum balance, both necessary conditions for 2-body decays. To identify the decay as a K decay one can then use the Cherenkov counter signals and range measurements to identify the particles and thus the masses of the secondaries. The invariant mass of the two particle system can be easily computed and compared with the total initial energy, the mass of the kaon:

$$m_{12}^2 = m_1^2 + m_2^2 + 2\ (E_1\ E_2 - p_1\ p_2\ \cos\theta_{12}).$$

There are several decay modes of the K_L^o which can be mistaken for the 2 lepton modes if errors are made in the reconstruction of the event. $K_{\ell 3}$ decays, $K_L^o \rightarrow \pi\mu\nu$ and $K_L^o \rightarrow \pi e\nu$, can look like 2 lepton modes if the neutrino has little energy and the pion is either misidentified or decays into a muon. Fortunately, the probability that the neutrino in the $K_{\ell 3}$ decays will have a low center of mass energy is relatively small. Figure 4 shows the neutrino energy spectrum as calculated using standard V-A weak interaction theory. By making the trigger scintillators narrow enough, requiring decay products to be nearly parallel to the beam after the magnets, $K_{\ell 3}$ events with neutrino energies greater than a few MeV were not detected by the trigger system.

The pion from $K_{\ell 3}$ events can decay in the magnet spark chamber system and cause the bending angle to change and the momentum to be mismeasured. Scattering can also cause the same mismeasurement with any of the particles involved.

To reduce the possibility of a scattering error, the decay volume and spectrometer system were filled with helium. Also, the spark

chambers were constructed of 3 mil diameter aluminum wire and the interfaces between the spark chambers and helium containers were special membranes of 1 mil mylar coated with 1500 Å aluminum. Most important, the entire scintillation trigger system was placed downstream of the spark chambers.

Finally, to measure the number of K_L^o decays occurring in the decay volume the relatively rare, but well-measured, CP-violating two pion mode was monitored. With the line integral of the magnets adjusted to the $K_{\mu\mu}$ transverse momentum, the detection efficiency for the $K_{\pi\pi}$ mode was approximately 70% of the efficiency for detecting each of the three $K_{\ell\ell}$ modes.

III. EXPERIMENTAL APPARATUS

A. Trigger Elements

1. Hodoscopes

Each secondary was required to be approximately parallel to the beam centerline after passing through the magnet. This was accomplished on each side of the apparatus with two scintillation counter hodoscopes placed 98" apart immediately after the last spark chamber. Figure 3 shows the spatial orientation of the four hodoscopes with respect to the neutral kaon beam. Each front hodoscope had 28 – 1.5" wide by 42" high vertical scintillation counters or staves and each rear hodoscope had 30 – 1.512" wide by 52" high staves. The slightly larger width of the rear counters was to compensate for the ± 1° horizontal divergence of the kaon beam. The front staves were 1/4" thick (in the beam direction) Pilot Y scintillator and the rear staves were 1/2" thick Pilot Y. RCA 6810 photomultipliers were used on the front and RCA 6655 tubes on the rear hodoscopes. No light pipes were used; each stave was equipped with one tube which made contact at the end of the scintillator.

The stave numbering system, important in understanding the coincidence requirement, was simply 1 to 28 or 30, for front or rear respectively, with numbers increasing outward from the neutral beam. The hodoscopes were aligned so that counter 1 in front and 1 in the rear defined a trajectory parallel to the neutral beam centerline.

Except for counters at the edges of the hodoscopes the signal from each front stave was put into coincidence with the signals from 6 rear staves. Each of these 6 coincidence possibilities corresponded to a horizontal angular interval of about 15 milliradians for the secondary downstream of the magnet. In actual practice it was possible to add the signals from coincidences from all 28 front staves and their respective rear staves such that there were only 6 output signals. These 6 signals, called column outputs, corresponded directly to a trajectory's horizontal divergence after the magnet independent of which front stave it passed through.

Computer calculations which considered the K beam momentum, angular divergence, and decay distributions indicated that equal triggering efficiency for the $K_{\mu\mu}$, K_{ee}, and $K_{\mu e}$ modes was possible with only about 30% loss of efficiency for the normalizing $K_{\pi\pi}$ mode. That is, if the magnets were set to the p^* of the $K_{\mu\mu}$ mode (225 MeV), for each front vertical stave the six rear staves in the coincidence had sensitivities as shown in Fig. 5.

2. Matrices

The actual coincidence matrix was constructed from MECL II[11] logic units. Two identical units were used, one for each side of the apparatus. Front and rear counter signals were fed into the matrix unit discriminators and the shaped output pulses were put out onto the matrix lines such that a coincidence chip was located at every desired intersection. See Fig. 6.

The outputs from the coincidence chips were arranged in six columns, each of which corresponded to an angular interval for the particle trajectory after the magnet. Each time counter i in the front and i + 2 in the rear were in coincidence, for example, a signal would be sent down column 6. This particular column would correspond to a transverse momentum consistent with K_{ee} decay mode.

3. Other Scintillators in the Trigger

Six horizontal staves about 6" wide placed to cover the active area of the vertical counters were mounted on each front hodoscope frame. These were also made of 1/4" thick Pilot Y scintillator and were equipped with special bent strip light pipes which allowed each of them to be viewed by a single RCA 6810 photomultiplier. Their purpose was mainly to provide protection against accidental triggers due to noise in the front vertical staves. These counters also aided the event reconstruction.

One particular problem with the K beam used in this experiment was a neutron flux almost three orders of magnitude larger than the K_L^o flux. Many unwanted triggers came from neutron-helium interactions. Often a proton from such an interaction and an associated pion satisfied the angular trigger requirement. However the slower protons could be discriminated by a time-of-flight measurement. Unfortunately, the MECL II logic used in the matrix units had a resolution of about 45 ns, and an additional pair of counters had to be added to do fast left-right coincidences on the two arms of the spectrometer. These counters and their associated electronics were called chronotrons

although they did not measure time as a chronotron usually does, but were designed to produce an output pulse insensitive in time to the position of the trajectory on the face of the counter.

Each fast counter was constructed from a 4' x 4' x 3/4" sheet of Pilot F scintillator with light pipes attached as shown in Fig. 7. The signals from the two top photomultipliers were added, as were the signals from the two bottom tubes. These added signals were each discriminated and shaped (to a width of about 3 ns) and fed into the opposite ends of a special coaxial cable. At intervals of 6" the center coaxial conductor was connected to diodes biased such that they conducted only when the pulse amplitude corresponded to the sum of the signals from the top and bottom of the counter. In this way, the output timing of the chronotron was independent of the altitude of the incident particle's trajectory. This system was tested with a movable telescope and the output from the chronotron was found to vary at most by about 1 ns for particles anywhere on the face of the scintillator.

The outputs from the right and left chronotrons were again discriminated and shaped (to a width of ~ 5 ns), put into coincidence and added to the trigger requirement. The timing and reliability of these counters were periodically checked by running with the chronotron requirements out of the trigger and comparing the number of $K_{\pi\pi}$ events reconstructed to those in similar runs with the chronotron coincidence required.

The actual spark chamber trigger coincidence required five signals. One signal from each of the two matrix units was required as was a signal from each of the two sets of six horizontal staves. The fifth requirement was the signal from the fast left-right chronotron coincidence. The five fold coincidence output simultaneously fired the spark chambers, sent out strobes to the individual photomultiplier flip-flops, and started the master read-out control.

In order to tell which counters were involved in an event, all photomultipliers with the exception of the independent target and neutron monitors were equipped with 100 ns delay cards after the discriminators. The discriminator outputs were divided and signals were sent to the delay cards and logic units at the same time. Thus if a spark chamber coincidence occurred, the strobe signal could be used with the delayed counter signal to set a flip-flop. The state of these flip-flops was recorded by the readout system and so all of the counters which were involved in each event was known.

B. Momentum Analysis

1. Magnets

Two magnets were specially constructed for this experiment to satisfy the stringent requirement of the trigger system that the line integral be constant over the total aperture. The coils were borrowed from a standard low power H magnet, and the coils and new iron were so arranged as to make what is known as a picture frame magnet. By shimming the iron and working the coil packages as close together as possible an aperture 25" high and 36" across was obtained. The line integral was

constant to better than one percent for 95% of the expected orbits in the experiment. Figure 8 shows a line drawing of one of these magnets.

Both magnets were tilted 6° with respect to the neutral beam centerline to increase the solid angle for the expected 2-body K decays. The detection efficiency also increased with magnet aperture proximity to the neutral beam. For this reason notches were made in the beam side yokes of each magnet and lead wedges were attached to the sides of the magnets. The magnets were then placed as near to the neutral beam as possible and the lead wedges acted as absorbers for the fringes of the neutral beam.

The line integral uniformity was a great help in the event reconstruction. In fact, one look-up table of momentum vs. bending angle with 60 entries parameterized both magnets well enough to measure the invariant mass of the two secondaries to ± 1/3%.

The absolute normalization of the magnetic field was done using the $K_{\pi\pi}$ events, because the field measurements had been made before the iron spark chamber support frame was installed. Flux-robbing by the support frame reduced the average line integral by about 1.4% although the overall shape of the field apparently remained the same as in the initial field maps judging by the success of the momentum parameterization.

Magnetic shields were necessary because the fields at the spark chambers nearest the magnets were too large for practical usage of magnetostrictive readout. Iron plates 1" thick were fitted to both sides of each magnet with rectangular holes cut in them just large

enough to let the secondary particles through. Four inch iron channel was welded onto the perimeter of the hole to further reduce the magnetic field beyond the iron plate.

2. Spark Chambers

Because of the momentum resolution requirements of the experiment, the spark chambers had to be constructed with as few radiation lengths of material as possible. Each spark chamber had four planes of 3 mil diameter aluminum wires spaced 1 mm apart. Magnetostrictive readout[12] was used and each chamber gave two x and two y measurements for each particle passing through.

Each spark chamber's planes of wires made up two gaps of 3/8" with the two inside planes of wires, separated by only 2 mils of mylar, sharing the high voltage pulse. Figure 9 shows the orientation of the wire planes and their relationship to the magnetostrictive pick-up wires. The pick-up wires were mounted on aluminum bars with the sensing coil and preamplifier at one end. These bars or wands fitted into slots milled in the NEMA G10 fiberglass frames and were held tightly against the spark chamber wires with teflon coated springs.

There were two chamber sizes; the active areas were 40.5" horizontal by 29" vertical in the front 4 chambers and 42.5" x 37.5" in the last six chambers. The next-to-last chambers were rotated 10 degrees in the plane of the chamber to help resolve ambiguities in case of multiple trajectories.

All chambers were supported and held in place by a steel platform which was one structural unit extending from the front spark chambers, below the magnets, to the rear spark chambers. The spark chambers slid in and out on steel bars held by the support platform. The steel bars

were aligned and shimmed to lie in a plane before the final magnet and spark chamber support assembly was made. Final spark chamber alignment was done with straight tracks from periodic runs with the magnets off. The rms deviation for sparks on fitted tracks varied from 20 to 40 mils depending on the chamber operating conditions.

Each chamber had one spark gap attached to the top corner opposite the K beam. The trigger electrode was an easily-replaced Champion spark plug which was pulsed by a master spark gap developed by the LRL PIG[13] group. The Sprague 4000 pf capacitors on each chamber spark gap were charged to about 12 KV with a special charging system developed for this experiment. This system featured a one ms delay before recharging began and a 0.2 ms recharging time. The high voltage on the central spark chamber planes was about 4 KV with a rise time of about 60 ns (10% to 90% amplitude) and pulse length of about 120 ns (FWHM).

The chambers were operated with the usual 90% neon - 10% helium mixture and doped with ethyl alcohol at 10% of total vapor saturation concentration. The amount of alcohol in the chambers changed their performance drastically. For example, no sparks would form at normal operating voltages without alcohol. If the alcohol concentration became larger than about 15% the chambers tended to spark in places not associated with the particle trajectories.

The concentration of alcohol was held constant by bubbling 10% by flow rate of the neon-helium through a bottle of ethyl alcohol held at $19^{\circ} \pm 2^{\circ}$ Centigrade. After the gas passed through the chambers the alcohol and other impurities were removed with liquid

nitrogen trap and the gas was recirculated through the alcohol and chamber system. All chambers were fed in parallel and the flow rates were such that the gas was exchanged in something less than an hour.

Diodes on the chamber spark gaps allowed a d.c. clearing field to be applied across the chamber; for the 10% alcohol mixture a value of 70 volts was generally used. Also a pulsed clearing field of about 1 KV was applied for one ms a few ms after each firing to help clear the gas of spark remnants.

3. Readout

The magnetostrictive readout system was of conventional design in most respects. Each wand picked up two signals from fiducial wires mounted on the chambers at the ends of the wand. These signals bracketed the signal from the spark. The wand pick-up wire was polarized with a permanent magnet and currents passing through the nearby fiducial or spark plane wires caused a sonic pulse to propagate down to the end of the wand. Typical speeds were 200 μs/meter. At the end of the wand the sonic pulse was picked up by a coil and pre-amplifier. The ratio of the time between the first fiducial signal and the spark and the time between the first and last fiducials measured the position of the spark relative to the physical distance between the two fiducials.

The times between successive sonic signals were measured with Scientific Accessories Corporation (SAC) digitizers. These devices consisted of a set of scalers for each wand and a 20 MHz clock. The pulse from the first fiducial turned on all the scalers in a set which then counted the 20 MHz clock. Successive wand signals turned off

the rest of the scalers in order. These scaler readings were written on magnetic tape for later analysis.

The chambers upstream of the magnets were more exposed to secondaries from neutron and γ interactions than those downstream. For this reason the front chambers used 6 scalers per wand and could then measure a maximum of 6 sparks while the rear chambers had only 4 scalers per wand. Although the SAC boxes were equipped with their own discriminators, the range of amplitudes of preamp pulses was large enough to require the use of zero-crossing discriminators to get the best possible resolution.

The wand signals were continuously monitored with an oscilloscope as there were problems with the pick-up wire becoming depolarized and therefore less sensitive to the spark signal. The observed depolarization seemed to be due to stray magnetic field from the magnets and the steel spark chamber support frame. When the picture frame magnets' polarity was reversed many of the wands near the magnets had to be repolarized.

4. Helium System

The helium system extended from the upstream end of the last sweeping magnet to the last spark chamber. Each interface between the spark chambers and helium containers was made with 1 mil thick mylar coated with 1500 Å of aluminum. This special material was originally ordered as a means for putting a clearing field between the ground planes of the spark chambers and the neon helium container wall. The clearing field was found not to be needed but the aluminum coated mylar had 1/10th the helium diffusion rate of the uncoated material. While the diffusion rate would have meant a considerable loss of helium the

real problem was that the helium would diffuse into the spark chamber gas and change the neon-helium ratio.

The thin membranes were susceptible to damage from errors in pressure regulation but the problems were not really too great. The pressure was easily regulated to ± 0.05 inches of water. Relief valves were also used. The upper spark chamber supports were made of 6 inch diameter pipe which served as a helium manifold to feed all of the boxes in parallel. The helium was recirculated through a liquid nitrogen trap in a system similar to that used for the neon to insure the purity of the gas.

C. Particle Identification

The signals from both the Cherenkov counters and range counters were not used in the trigger. All photomultiplier signals from these identification devices were recorded with each event.

1. Cherenkov Counters

Electrons were detected with two Freon 12 Cherenkov counters placed between the hodoscopes. The small angular divergence of the secondary particles (± 45 mr) implied that these counters could be constructed with fairly simple focal properties. A spherical lucite mirror in each counter reflected the Cherenkov light back to three RCA 4522 photomultipliers on the top of the counter. See Fig. 10. The focal length of the mirror was 100". Light collection efficiency at the photomultipliers was increased by using paraboloidal light cones.

These counters were tested in a parasitic beam at the Bevatron and found to be better than 99.5% efficient over most of the area defined by the trigger system.

Analysis of events taken from normal running conditions of K_{e3} events has shown that about two percent of the pions counted in the Cherenkov counters. This pion "breakthrough" may have been caused by delta rays produced by the pions, accidental coincidences from other particles, or scintillation in the Freon 12.

2. Range Boxes

A schematic of one of the range determination systems is shown in Fig. 10. Each system consisted of a carbon block followed by a box containing layers of iron and scintillator. In the analysis, strongly interacting pions were distinguished from muons by typically having less penetration into the carbon and steel of the range box. Muons, interacting only electromagnetically, had ranges well defined by their measured momenta. Although the ranges of pions and muons of the same momentum are different because of ionization energy loss, in this experiment the less subtle differences due to nuclear attenuation were used to distinguish the two types of particles in the events of interest.

Carbon was used instead of iron in the first stage because it has higher nuclear absorption for a given range of material. Considering the expected pion momenta, the carbon was expected to stop 89% of the incident pions while an equivalent range of iron was expected to stop 82%.

Behind the carbon block were 17 scintillators with 4' x 4' x 1" plates of steel arranged to give the best possible resolution to the device. The scintillator-iron pattern is shown in Fig. 10.

Sheets of 3/4" thick 4' x 4' Pilot F scintillator were used in the first eight positions and sheets of Nuclear Enterprises 102 scintillator of the same size were used in the last 9 positions. The Pilot F scintillator worked very well with only one Amperex 56 DVP tube placed in a corner as shown in the detail of Fig. 10. Because of greater light attenuation in the plastic the NE 102 scintillator required two tubes each placed on a top corner. Tests on all scintillators in a Bevatron test beam indicated that the Pilot F could be expected to be at least 99.99% efficient even at the least efficient spot on the face of the scintillator. The NE 102 was slightly less efficient even though equipped with an extra tube.

Actual tests of the characteristics of the range boxes were made using samples of $K_{\mu 3}$ events. In the analysis the measured range of a particle was taken to be defined by the last two adjacent counters which fired. This was necessary because of occasional accidentals in the downstream scintillators.

D. Data Acquisition and Storage

The standard LRL-NIDBUS[14] system interfaced with a Digital Equipment Corporation PDP-9 computer was used to read and store events, each time the spark chambers fired. The trigger logic box was the starting point for the information system. If the usual requirements

of beam spill, computer ready and H.V. ready were met it could respond to the fulfilled trigger requirements by sending out three signals. One was the counter strobe, another the master spark chamber trigger which fired the spark gaps on the individual chambers. The last was to the NIDBUS Master Control.

The Master Control zeroed and enabled the SAC boxes, paused to let them digitize the wand signals, then read and sent the information from all of the scintillators and wand scalers to the PDP-9. This information went via the data channel rather than through the accumulator so the computer could continue to check previous events during the data transfer.

The operating program made various checks on the data, notified the experimenter if anything was abnormal, and wrote the events accumulated in the event buffer on magnetic tape if the buffer were full.

The event checking included comparing each set of wand scalers for consistency. Besides checking for monotonically increasing scaler readings and zero readings, the program also looked for a scaler reading corresponding to the distance between the two fiducial wires on the chamber. This was the most important data check the computer did; by comparing the scalers to a table of fiducial numbers, it found such things as bits stuck in the SAC box scalers, bipolar wand pulses caused by stray magnetic fields, and early starts in the scalers due to errors in gating or noise on the input lines.

Histograms of hodoscope counters involved in spark chamber triggers were kept and could be displayed by setting sense switches on the

computer. By looking for continuity in these histograms one could continuously monitor the relative efficiency of the counters.

Because each chamber gave two x and two y measurements it was easy to check for efficiency by looking for pairs of sparks with the same coordinate. The percentage of these doubles was a good indication of the whole system's effectiveness. Some of the problems discovered with doubles percentages included gas line constrictions, wand depolarization, clearing field diode failures, and SAC box scaler failures.

Sense switches also allowed the display of one event per Bevatron pulse on a CRT screen. All 40 wand signals and all hodoscope counters were arranged to represent the event topologically. Range box and Cherenkov counter signals were also displayed. Figure 11 shows the proverbial typical event. This display was useful for finding chamber breakdowns and monitoring the percentage of kinematically reconstructable events under the various running conditions. One could also choose which of the events of the Bevatron spill to be displayed. This was in case the beam conditions changed during the spill, and to see if the chambers were not recovering fast enough between firings.

It should be emphasized that all errors discovered by the computer were immediately made known to the experimenter. In fact, the prompt discoveries made by the PDP-9 of faults in the apparatus were essential to the efficient operation of the experiment.

Under normal operating conditions a data tape was filled in 2 to 4 hours. These tapes were then taken to the CDC 6600 computer where

they were subjected to a more detailed error analysis. The 6600 programs, in addition to doing the same kinds of scaler checks as the PDP–9, checked for spark chamber movement, provided more permanent histograms and provided decay vertex plots for background monitoring.

The final data tapes were also copied onto the LRL Photodigital Mass Storage System[15] for permanent storage and easy retrieval.

E. Neutral Beam

The production target was located at the Channel I 3rd focus of the external proton beam (EPB) of the Bevatron. Most of the running described in this paper was done with one of two targets; one copper .2" wide x .1" high x 5" in the EPB direction, the other platinum .2" x .1" x 2". The proton beam had between 1 and 5 x 10^{11} protons per pulse for most of the running and a kinetic energy of 4.8 GeV.

A diagram of the neutral beam collimation system is shown in Figs. 12a and 12b. The neutral beam was taken from the production target at 3.7° downward. This angle was chosen to be safely away from the large proton charge–exchange diffraction peak. Also it had the safety feature that if the EPB backstop magnet failed, the proton beam was stopped by the shielding and could not come directly into the experimental area.

Although the downward angle did lead to loss of leg room at the downstream end of the spectrometer (see Fig. 10), it did provide left–right symmetry for the total beam–spectrometer system.

The horizontal uranium collimator near the beginning of the beam line was remotely adjustable and was very useful for initial beam studies. It was also used to compensate for changes in intensity or focusing of the EPB. The jaws of this collimator determined the width of the beam; with the adjustable collimator wide open the beam was 19.5" wide and 24" high at a point 50' from the target, exactly between the two picture frame magnets.

In actual practice the background in the front spark chambers from neutron-helium interactions limited the data rate. The normal operating conditions were with the adjustable collimator about 5/9 open and 1 or 2 x 10^{11} protons per pulse on the target. In this configuration about 3 x 10^{4} K_L^o per pulse passed through the decay volume. This caused trigger rates of 10 to 20 per pulse.

The most effective sweeping magnet was the EPB backstop magnet X1M7. The next magnet M1 swept vertically and further reduced the charged particle counting rates in the hodoscopes by 30%. The last sweeping magnet made little difference in scintillator rates but did seem to reduce the average number of sparks per event in the front spark chambers by 10 to 20%.

The 1.2 millisteradian beam was the largest neutral beam ever used at the Bevatron. Neutron fluxes of nearly 10^{9}/sec with 5 x 10^{11} protons per second on the target caused large backgrounds in scintillators even when air was the only material the neutrons passed through.

The decay volume helium box helped reduce neutron interactions which caused charged secondaries to go through the picture frame

magnets. Adding helium containers downstream of the picture frame magnets did not help very much, but 6" steel plates placed on both sides of the beam there helped reduce background in the counters. These plates extended from the shields of the picture frame magnets to the range boxes. To reduce accidental counts coming from the beam stop a re-entrant cavity 15' deep was formed from concrete blocks to stop the beam.

The EPB intensity was monitored with a secondary emission monitor (SEM) placed upstream of the target. The few mils of aluminum in this monitor was large enough that interactions with the halo of the EPB caused neutrons which escaped the primary collimation system to interact at the top of the last sweeping magnet. Charged particles from these interactions caused spurious sparks in the front chambers and necessitated moving the SEM several feet upstream of the target. Even with the SEM moved 10 feet upstream of the target, off-axis neutrons were still produced in the target area by the halo of the proton beam. A foot-long, vertical uranium collimator, the mini-collimator, was placed behind the EPB backstop magnet to help stop these neutrons. This reduced the beam solid angle by about 25% but because of the limited vertical apertures of the picture frame magnets it reduced the useful kaon flux only slightly for coplanar decays.

The amount of beam hitting the target was monitored with a 3-counter telescope (IM) which looked directly at the target. Also two neutron counters (see Fig. 3) sat directly in the neutral beam at the entrance to the backstop cavity. These monitors were not used for normalization but rather for checks on the stability of beam conditions.

IV. DATA ANALYSIS

A. Event Reconstruction

The laboratory coordinates of the fiducial wires in each spark chamber were originally determined with standard surveying techniques. Consistency was checked and fine adjustments were made with events taken with the magnets turned off. Given the fiducial coordinates the real space interpretation of the wand signals followed with simple interpolation.

In the following discussion x and y measurements correspond to horizontal and vertical displacements, respectively. Since no diagonal wires were used in the chambers the x and y wand signals were independent. For example, 6 sparks would give 6 horizontal wand signals and 6 vertical wand signals which implied 36 possible spark positions. Although more than 4 sparks in a chamber was rare it was clear that permuting coordinates for 40 wands would be very time consuming.

The association of the wand signal coordinates into lines consistent with possible trajectories was simplified by requiring that there be at least one x and one y coordinate from each chamber along a trajectory. Use of the hodoscope information also simplified the reconstruction.

Each arm of the spectrometer was treated independently before the decay vertex was tested. The technique was to use the staves in the trigger to define acceptable areas in the rear spark chambers. Then if a trajectory were found in the last three chambers, it was extended forward through the magnets to help define acceptable areas in the two front chambers.

For each side, the vertical staves in the trigger defined an acceptance corridor in the three chambers behind the magnets. All x-coordinates in the corridor were permuted to find possible fits to a straight line. The real space x coordinate in the rotated middle chamber depended on both the x and y wand coordinates. The best combination of the x and y wand signals in the rotated chamber for the three chamber straight line fit was used. This then determined the real space position of the sparks in the rotated chamber.

The horizontal stave in the trigger and the real space y coordinate in the rotated chamber defined acceptance areas for all y measurements in the other rear chambers. All accepted rear y measurements in these other chambers were then permuted for straight line fits. The straight line fits were required to have a χ^2 per degree of freedom of ≤ 3 for the 6 spark tracks. The rms deviation was assumed to be 50 mils which was slightly larger than the worst case observed.

The intersection of downstream trajectories and the midplane of the magnet defined a spot which was then used to form possible tracks in the front chambers. The y projection of the trajectory behind the magnet with a small correction for vertical focusing of the magnet served to define the y coordinate acceptance corridor in the front chambers. The spot on the midplane and the decay volume limits were used to define an acceptance corridor for the front x-coordinate measurements.

All possible spark interpretations in the front corridors which gave trajectories within 1" of the magnet midplane spot were analyzed.

The front trajectories on the two sides of the apparatus were then tested for an acceptable vertex in the decay volume. The intersection of the right and left front trajectories in the x–z plane (z is the beam direction) defined the decay point. The two y values, YD1 and YD2, were calculated for the trajectories at the decay point. The average of YD1 and YD2 was used to test if the event took place in the decay volume. The difference, YD1–YD2, was used to check the validity of the event.

Figure 13 shows the distribution of distances between the trajectories at the decay point for all accepted $K_{\pi\pi}$ events. The actual cuts on the events varied from 0.5" to 0.8" depending linearly on whether the decay was at the downstream or upstream end of the decay volume.

Events were eliminated if a trajectory came to within about 1/2" of the wall of the helium box which lined the magnet.

B. Reduction to 2–Body Final States

Events with at least one complete trajectory in each arm of the spectrometer and an acceptable vertex were considered 2–body candidates. If there were more than one trajectory on a side each was tried for the best two–body fit.

The measured momenta and positions of the secondaries and the decay vertex were used to project the parent particle's path back to the target. The distance of closest approach of the parent trajectory to the target was then used to further eliminate spurious events. All 2–body candidates with parents having an apparent origin within 2.4" of the target and having an invariant mass within 20 MeV of the mass of the

kaon were stored in raw form. Both pion and muon identities for the secondaries were tried in forming the invariant mass unless Cherenkov signals defined the particles as electrons.

The condensation reduced the data sample from about 1.3 million events to about 40 thousand and took 10 hours on the CDC 6600 computer. The target limits and the invariant mass limits were chosen to eliminate spurious two body events caused by $K_{\ell 3}$ decays and yet not allow any possible 2 body events to be lost.

Figure 14a shows the distance of closest approach to the target for all reconstructed events in the condensed sample. All events originating within 2" of the target were used in the final analysis of the next section.

C. Normalization Sample

The number of $K_{\pi\pi}$ events monitored directly the number of kaons which decayed in the decay volume. Figure 15a shows the invariant mass of all events without Cherenkov signals in the condensed data sample which gave an invariant mass within 20 MeV of the kaon mass when interpreted as $K_{\pi\pi}$.

1. Resolution

Considering the momentum distribution of the secondaries from the sample above, any pion from the $K_{\pi\pi}$ events had about a 13% chance of decaying before leaving the momentum analysis system. A more accurate measurement of the invariant mass resolution for the two lepton decay mode was possible if pion decays-in-flight were eliminated from the $K_{\pi\pi}$

sample. Figure 15b shows the invariant mass plot for those $K_{\pi\pi}$ candidates which had neither secondary penetrating through the carbon degrader. These events, although they have a lower kaon momentum and thus worse resolution due to multiple scattering, were less likely to have decays in flight. These events also have less contamination due to $K_{\mu 3}$ events and the shape of the peak is more easily seen.

Figure 15b then represents the invariant mass resolution for the two-lepton decay modes, which also should suffer no loss of resolution due to decays in flight. The rms deviation is about 1.5 MeV. The distance of closest approach to the target of the parents of the events in Figure 15b is plotted in Fig. 14b.

2. Background Subtraction

Both $K_{\mu 3}$ and K_{e3} events could be mistaken for $K_{\pi\pi}$ events. Incorrectly identified secondaries in the three body decays could lead to an invariant mass near the K mass. However, Monte-Carlo investigations showed that events of this type would contribute a fairly smooth background. Figures 16a and 16b show the straight-line, eyeball fits to the backgrounds for data taken at the $K_{\mu\mu}$ and $K_{\pi\pi}$ magnet settings, respectively. More elaborate fits did not seem appropriate as approximately 5% of the $K_{\pi\pi}$ events were expected to be completely lost due to decays in flight before this stage in the analysis.

3. Detection Efficiency

All data used in this analysis were taken at two magnet settings; one at the transverse momentum of the $K_{\mu\mu}$ mode and the other at that of the $K_{\pi\pi}$ mode.

The efficiency of the detection system for a particular two body decay mode with the magnets set at a certain transverse momentum was easily measured. Using the independent target monitor for normalization

and taking runs at different magnet settings, the number of $K_{\pi\pi}$ events found could be compared to the number expected. The number expected was based on the $K_{\pi\pi}$ rate with the magnets tuned to the $K_{\pi\pi}$ setting. By taking 28 runs with both $K_{\pi\pi}$ and $K_{\mu\mu}$ magnet settings intermixed to eliminate any systematic errors the efficiency for detecting $K_{\pi\pi}$ events at the $K_{\mu\mu}$ magnet setting was measured to be 69% ± 5%.

That is, at the $K_{\mu\mu}$ setting there were about 960 $K_{\pi\pi}$ events while the number of $K_{\pi\pi}$ events at the $K_{\pi\pi}$ magnet setting renormalized with the independent monitor indicated that 1395 should have occurred. The missing events were from low momentum kaons which had secondaries deflected inward due to the higher magnetic field at the $K_{\mu\mu}$ setting.

This method of measuring the relative detection efficiencies of the apparatus for different magnet settings and for different decay modes is only good to a few percent due to the slightly different average opening angles for the different two body decay modes.

The same technique was used to measure the detection efficiency for K_{ee} events taken with the magnets set at the transverse momentum of the $K_{\pi\pi}$ mode. In this case, the magnets were set to $p^* = 171$ MeV/c to allow the $K_{\pi\pi}$ events to simulate K_{ee} events decaying with the magnets at the $K_{\pi\pi}$ setting. The result of this measurement was that 85% ± 15% of the K_{ee} events would be seen with the magnets at the $K_{\pi\pi}$ setting. Although this number was not measured very accurately, only about one-tenth of the data was taken at the $K_{\pi\pi}$ magnet setting and the final results were correspondingly insensitive to the precise value.

The number of $K_{\pi\pi}$ events at the $K_{\pi\pi}$ magnet setting was 2450 and at the $K_{\mu\mu}$ magnet setting the number was 20600. These numbers are taken from figures 16a and 16b. Correcting for detection efficiency for $K_{\pi\pi}$ at the $K_{\mu\mu}$ magnet setting these numbers combine to give an effective total of 32250 $K_{\pi\pi}$ events.

D. Two Lepton Candidates

Both $K_{\mu\mu}$ and $K_{e\mu}$ candidates were accepted from the two body sample only if the muons stopped within 3 cells of their expected range in the range box. The expected range was determined from standard range tables and tested using reconstructed $K_{\mu 3}$ events.

Figure 17 shows the invariant mass distribution of the final 2 lepton candidates after the 3 cell cut was made. There were no K_{ee} candidates within 20 MeV and no $K_{\mu e}$ candidates within 11 MeV of the mass of the kaon.

The two $K_{\mu\mu}$ candidates with an invariant mass above 485 MeV were examined to see if they were $K_{\mu 3}$ events in which the pion had decayed in flight. Ordinarily such a decay could not produce such a large increase in the invariant mass. However if the pion decayed in or near the magnet the bending angle could be mismeasured. The simple magnet parameterization was insufficient to test for these decays in flight and orbits had to be traced through the magnets using the measured fields.

To test the validity of the orbits, secondaries from the $K_{\pi\pi}$ sample which stopped before the range box were used. From this restricted $K_{\pi\pi}$ sample, secondaries were chosen which had the same

orbit characteristics as the $K_{\mu\mu}$ candidates. All such $K_{\pi\pi}$ trajectories within 3" of the magnet midplane spot, within 20 mr of the dip angle, and within 20 mr of the bending angle of the incident $K_{\mu\mu}$ candidate trajectory in question were traced through the magnets.

Both of the $K_{\mu\mu}$ candidates had one trajectory with a range shorter than the expected muon range by 1 cell of the range box. These trajectories and the associated $K_{\pi\pi}$ trajectories were compared for the two $K_{\mu\mu}$ candidates. Figure 18 shows the difference between the predicted and actual x value of the midplane spot for the rear trajectory for all orbits. The dark squares represent the $K_{\mu\mu}$ candidates. The predicted value was determined by starting from the trajectory in front of the magnet and integrating through the field. When the trajectory had passed through the field a new midplane spot was predicted by tracing a straight line back from the orbit to the magnet midplane.

Both $K_{\mu\mu}$ candidates were consistent with $K_{\mu 3}$ decays with the pion decaying in or near the magnet. The one candidate with an invariant mass near the Kaon mass, for example, had a 2-1/2 standard deviation magnet midplane spot discrepancy and stopped 1 cell short of its expected muon range.

E. Results

If one event of each of the leptonic modes had been found, the branching ratios relative to the $K_{\pi\pi}$ mode would be

$$\frac{\Gamma\,(K_L^o \to \ell^+ \ell^-)}{\Gamma\,(K_L^o \to \pi^+ \pi^-)} = \frac{1}{32200}$$

Using the measured value for the $K_L^o \to \pi^+ \pi^-$ branching ratio the total branching ratios based on one event would be

$$\frac{\Gamma (K_L^o \to \ell^+ \ell^-)}{\Gamma (K_L^o \to \text{all})} = 4.9 \times 10^{-8}$$

The probability of finding n events when x events are expected is given by a Poisson distribution.

$$P(n) = \frac{e^{-X} X^n}{n!}$$

The probability of seeing 0 events when 1 is expected is $e^{-1} = .37$. Thus the probability that the above branching ratios are smaller than the actual values is 37%. Alternatively, these branching ratios represent upper limits at a 63% confidence level.

The customary confidence level is 90%. To have 10% probability of seeing 0 events, the expected number must be $X = \ell n_e\ 10 = 2.303$. Thus the 90% confidence levels are 2.3 times those above or

$$\frac{\Gamma (K_L^o \to \ell^+ \ell^-)}{\Gamma (K_L^o \to \text{all})} < 1.12 \times 10^{-7} \quad (90\%\ \text{C.L.})$$

V. CONCLUSION

A. Second Order Weak Interactions

The new upper bound set by this experiment on the $K_{\mu\mu}$ rate puts a new limit to the weak interaction cut–off, Λ. This parameter appears as the energy limit of the divergent loop integral of the diagram on page 3. Ioffe and Shabalin[6] calculate

$$\frac{\Gamma\,(K_2^o \to \mu^+ \mu^-)}{\Gamma\,(K^+ \to \mu^+ \nu\,)} = \left(\frac{G\,\Lambda^2}{(4\pi)^2}\right)^2 ; \quad G = \frac{10^{-5}}{m_p^2}$$

The 90% confidence level value for the $K_{\mu\mu}$ branching ratio limit implies $\Lambda \lesssim 52$ GeV (42 GeV for 63% C.L.). One interpretation of this result is that weak interactions involving energies near 50 GeV must exhibit new characteristics. This conclusion is somewhat analogous to the 250 GeV limit imposed by the electron–neutrino cross–section calculation mentioned in the introduction. The difference is that in the cross–section calculation the limit on Λ is the result of a contradiction between the energy dependence of the cross–section and the limits imposed by unitarity. In the $K_{\mu\mu}$ case a value for Λ appears as a contradiction between a calculated second order process and a physical measurement.

If the cut–off is due to electromagnetic interactions, as Ioffe and Shabalin suggest in their model of two charged intermediate bosons, the mass of the intermediate boson should be approximately one twelfth of Λ, i.e.,

$$m_W \lesssim 4.5 \text{ GeV for 90\% C.L.}$$

$$m_W \lesssim 3.6 \text{ GeV for 63\% C.L.}$$

B. Neutral Leptonic Currents

That evidence for the existence of neutral leptonic currents will be seen in the $K_{\mu\mu}$ decay mode is doubtful. The upper limit for the $K_{\mu\mu}$ branching ratio set by this experiment is very close to the predicted electromagnetic $K_{\mu\mu}$ rate.

The electromagnetic $K_{\mu\mu}$ branching ratio relative to all modes is probably greater than 5×10^{-9} and may be larger than 10^{-8}. If the experiment of Hyams, et al., which measured the $\eta^{o} \rightarrow \mu\mu$ rate, may be interpreted as indicating that the $K_{\gamma\gamma}$ form factor is anomolously large, the electromagnetically induced $K_{\mu\mu}$ branching ratio may be between 2 and 4×10^{-8}. The published results of Foeth et al. combined with the results of this experiment imply that the $K_{\mu\mu}$ branching ratio is no larger than 3.6×10^{-8} (63% C.L.).

There is the possibility that the effects of neutral currents are the same magnitude as the electromagnetic effects in the $K_{\mu\mu}$ decay mode. Perhaps the high $\eta^{o} \rightarrow \mu^{+} \mu^{-}$ rate is due to a neutral leptonic current. Such a conspiracy of nature would be particularly perplexing as the present uncertainties in the electromagnetic calculations preclude the required precision to separate the effects.

The $K_{\mu e}$ and K_{ee} modes, on the other hand, are not affected by uncertainties in the electromagnetic calculations. However the existence of the $K_{\mu e}$ mode would indicate a violation of the rule of separate lepton number conservation. And even if there were neutral currents this rule could still be valid.

The K_{ee} mode is still a likely place to observe neutral currents. However to have some hope of detecting this mode at the present level

of experimental sophistication, the vector-axial vector leptonic coupling must become scalar-pseudoscalar. That is, the new $K_{\mu\mu}$ limit and the relative rates calculated in Appendix A using V-A coupling set an upper limit for the K_{ee} branching ratio, i.e.,

$$\frac{\Gamma (K_L^o \rightarrow e^+ e^-)}{\Gamma (K_L^o \rightarrow \text{all})} < 2.7 \times 10^{-12} \text{ (90\% C.L.)}$$

This result not only depends on the V-A coupling but the form of the neutral currents used in the calculation. In the added neutral leptonic current in the Appendix A calculation the symmetry between the electron and muon current was assumed. If the K_{ee} rate is measured to be larger than the above upper limit and can be shown to be V-A, it would be a violation of electron-muon universality.

As a final comment, it must be noted that this experiment is being continued. The data represented by this analysis were taken before the Bevatron shut-down which started November 24, 1969. Data taking with a slightly different trigger scheme started again in February 1970. Hopefully, enough data will be collected eventually to allow branching ratio measurements near 2×10^{-9} for all three dileptonic K_L^o decay modes.

ACKNOWLEDGMENTS

I am very happy to acknowledge the enthusiasm and endeavor of the Lofgren research group members who participated in this experiment. Drs. Alan R. Clark, Tom Elioff, and R. Clive Field and their unique abilities were necessary elements of the research effort.

I would like particularly to thank Professor Leroy T. Kerth and Dr. William A. Wenzel not only for their participation in the experiment but also for the support and guidance they have given me in our years of association. In fact, it was by their example that I was initially inspired to enter graduate school in physics.

Thanks to Henry J. Frisch who, as the other graduate student working on the experiment, shared not only a dusty office but much hard work with me.

I would like to thank Chris Quigg for many helpful discussions.

This work was supported in part by the Alameda County Welfare Department and the Department of Agriculture Food Stamp Program.

This work was performed under the auspices of the U. S. Atomic Energy Commission.

APPENDIX A

As an example of the techniques used in calculating weak processes, the relative rates for the three possible neutral current elements of page 3 are calculated for K_L^o decay.

Ignoring the formal aspects of the theory (and the language of field theory: Lagrangian density, creation and destruction operators, etc.) a weak interaction matrix element can be written

$$M = \frac{G}{\sqrt{2}} jj^\dagger$$

where $G \cong \frac{10^{-5}}{m_p^2}$ and j and $j^\dagger$ include only the parts relevant to the particular matrix element in question.

A complete phenomenological form for j, consistent with all observations, is

$$j = \cos\theta_C \; J^H_{\Delta S=0} + \sin\theta_C \; J^H_{\Delta S=1} + j^\ell_{\Delta Q=1}$$

where θ_C is the Cabbibo angle, $j^\ell_{\Delta Q=1}$ is the ordinary charged leptonic current as on page 2, and $J^H_{\Delta S=0}$ and $J^H_{\Delta S=1}$ are the currents due to particles which also interact strongly. The S refers to strangeness, and the j and J are 4-component vectors.

If a neutral leptonic part is added with an angular suppression factor, j can be written

$$j = \cos\theta_C \; J^H_{\Delta S=0} + \sin\theta_C \; J^H_{\Delta S=1} + \cos\varphi \; j^\ell_{\Delta Q=1} + \sin\varphi \; j^\ell_{\Delta Q=0}$$

For $K_L^o \rightarrow$ lepton–antilepton the matrix element is

$$M = \frac{G}{\sqrt{2}} \sin\theta_C \sin\varphi \; J^H_{\Delta S=1} \; j^{\ell\dagger}_{\Delta Q=0}$$

The hadronic part of j is relatively unknown due to the masking effects of strong interactions and the best that can be done is to assume a phenomenological approach to $J^H_{\Delta S=1}$. If the neutral leptonic current were an ordinary current in the sense that it is a Lorentz four–vector, then $J^H_{\Delta S=1}$ must have four components to make M a Lorentz invariant. The only vector associated with the kaon is its four–momentum. Thus

$$J^H_{\Delta S=1} = f \psi P_K$$

where f is a form factor, ψ the kaon wave function and P_K the four-momentum of the kaon.

The complete matrix element for $K_L^o \rightarrow$ lepton-antilepton is

$$M = \left[\frac{Gf}{\sqrt{2}} \sin\theta_C \sin\varphi\right] \psi P_{K_\alpha} \bar{u}_1 \gamma_\alpha (1 + \gamma_5) u_2$$

where 1 and 2 refer to the antilepton and lepton. The notation is such that the Dirac equation is $(\not{p}-m)u = 0$ or $\bar{u}(\not{p}-m) = 0$ and the positive energy projection operator is $u\bar{u} = \not{p} + m$. Momentum conservation and the Dirac equation can be used to simplify M, i.e.

$$\begin{aligned} A &\equiv P_{K_\alpha} \bar{u}_1 \gamma_\alpha (1 + \gamma_5) u_2 \\ &= \bar{u}_1 P_{K_\alpha} \gamma_\alpha (1 + \gamma_5) u_2 \\ &= \bar{u}_1 (P_1 + P_2)_\alpha \gamma_\alpha (1 + \gamma_5) u_2 \end{aligned}$$

(contd)

(contd)

$$A = \bar{u}_1 (\not{p}_1 + \not{p}_2)(1 + \gamma_5) u_2$$

$$= \bar{u}_1 \left[m_1 (1 + \gamma_5) + (1 - \gamma_5) m_2 \right] u_2 \qquad \text{(A1)}$$

$$= \bar{u}_1 \left[(m_1 + m_2) + (m_1 - m_2) \gamma_5 \right] u_2$$

Case 1) For the $\mu\mu$ and ee modes this becomes

$$A = 2 m_\ell \bar{u}_1 u_2$$

Case 2) For the μe final state, the mass of the electron is negligible compared with that of the muon and

$$A = m_\mu \bar{u}_1 (1 + \gamma_5) u_2$$

The conjugate equation is

$$A^\dagger = m_\mu \bar{u}_2 (1 - \gamma_5) u_1$$

For Case 1), $m_1 = m_2$, the squared matrix element is

$$|M|^2 = \left[\frac{Gf}{\sqrt{2}} \sin\theta_C \sin\varphi \right]^2 \psi \psi^* (2m_\ell)^2 \left[(\bar{u}_1 u_2)(\bar{u}_1 u_2)^\dagger \right]$$

Implicitly summing over final spin states by using only the positive energy projection operators, the second term in brackets is

$$(\bar{u}_1 u_2)(\bar{u}_1 u_2)^\dagger = \bar{u}_1 u_2 \bar{u}_2 u_1$$

$$= \text{trace} (\bar{u}_1 u_2 \bar{u}_2 u_1)$$

$$= \text{trace} (u_1 \bar{u}_1 u_2 \bar{u}_2)$$

$$= \text{trace} \left[(\not{p}_1 + m_1)(\not{p}_2 + m_2) \right]$$

$$= 4 P_1 \cdot P_2 + 4 m_1 m_2$$

$$= 2 m_K^2$$

The last step follows from the kinematic relationship

$$2\, P_1 \cdot P_2 = (P_1 + P_2)^2 - P_1^2 - P_2^2$$
$$= m_K^2 - m_1^2 - m_2^2$$
$$= m_K^2 - 2\, m_\ell^2$$

And thus the final squared matrix element for a K_L^o decay into two leptons of the same mass is

$$|M|^2 = \left[\frac{Gf}{\sqrt{2}} \sin\theta_C \sin\varphi \right]^2 8\, m_\ell^2\, m_K^2$$

For Case 2), the μe mode,

$$|M|^2 = \left[\frac{Gf}{\sqrt{2}} \sin\theta_C \sin\varphi \right]^2 m_\mu^2 \left[(\bar{u}_1 (1 + \gamma_5)\, u_2)\, (\bar{u}_2\, (1 - \gamma_5)\, u_1) \right]$$

Summing over final lepton spins, by using the same proceedure as in the equal mass case, the second factor in brackets is

$$|\bar{u}_1\, (1 + \gamma_5)\, u_2|^2 = \text{trace} \left[(\not{P}_1 + m_1)\, (1 + \gamma_5)\, (\not{P}_2 + m_2)\, (1 - \gamma_5) \right]$$
$$= 8\, P_1 \cdot P_2$$
$$= 4\, (m_K^2 - m_\mu^2)$$

Thus for the μe mode,

$$|M|^2 = \left[\frac{Gf}{\sqrt{2}} \sin\theta_C \sin\varphi \right]^2 4\, m_\mu^2\, (m_K^2 - m_\mu^2)$$

Ignoring the common factor in brackets and using the phase space factor p, the K center of mass lepton momentum, the relative decay rates are

$$W_{\mu\mu} : W_{\mu e} : W_{ee} :: 2\, m_\mu^2\, (225) : m_\mu^2\, (.954)\, (238) : 2\, m_e^2\, (249)$$
$$:: 41400 : 20800 : 1$$

The form factor f has also been considered constant.

If the V-A (vector-axialvector) form for the leptonic current becomes S-P (scalar-pseudoscalar), the kaon four-momentum is replaced by a constant and $\gamma_\alpha(1 + \gamma_5)$ by $(1 + \gamma_5)$ in the expression for M. The Dirac equation used in Equation A1 is not needed and the calculations are the same as above except for the factors of the lepton mass. The transition probabilities are then simply proportional to phase space.

$$W_{uu} : W_{ue} : W_{ee} :: 0.90 : 0.96 : 1.00$$

REFERENCES

1. L. B. Okun', Weak Interactions of Elementary Particles (Pergamon Press 1965), p. 203.

2. Op. cit., p. 33.

3. Gasiorowicz, Elementary Particle Physics (John Wiley and Sons, 1966), p. 585.

4. A. Pais and S. B. Treiman, Phys. Rev. 176, 1974 (1968).

5. B. L. Ioffe and E. P. Shabalin, Soviet Journal of Nuclear Physics 6, 603 (1968).

6. M. Banner, J. W. Cronin, J. K. Liu, J. E. Pilcher, Phys. Rev. Letters 21, 1103 (1968).

7. C. Quigg and J. D. Jackson, UCRL-18487 (1968).

8. See the above report by Quigg and Jackson for a comparison and references.

9. B. D. Hyams, W. Koch, D. C. Potter, L. Von Lindern, E. Lorenz, G. Lütjens, U. Stierlin, and P. Weilhammer, Phys. Letters, 29B, 128 (1969).

10. H. Foeth, M. Holder, E. Radermacher, A. Staude, P. Darriulat, J. Deubch, K. Kleinknecht, C. Rubbia, K. Tittel, M. I. Ferrero and C. Grosso, Phys. Letters 30B, 282 (1969).

C. Rubbia, February 1970, private communication to R. C. Field. This new number is the result of an extended run using the same equipment as described in the previous reference.

M. Bott-Bodenhausen, X. De Bouard, D. G. Cassel, D. Dekkers, R. Felst, R. Mermod, I. Savin, P. Scharff, M. Vivargent, T. R. Willits, and K. Winter, Phys. Letters 24B, 194 (1967).

V. L. Fitch, R. F. Rota, J. Russ, and W. Vernon, Phys. Rev. 164, 1711 (1967).

- - - continued

10. - - - continued

U. Camerini, D. Cline, G. Gidal, P. Kalmus, A. Kernan, Nuovo Cimento 37, 1795 (1965).

U. Camerini, D. Cline, W. F. Fry, and W. M. Powell, Phys. Rev. Letters 13, 318 (1964).

R. Stiening, Announced at Bevatron Experimenters' Meeting, January 31, 1970.

D. Cline, Ph.D. Dissertation, U. of Wisconsin, 1965.

S. I. Parker, H. L. Anderson, and C. Rey, Phys. Rev. 133B, 768 (1964).

A. I. Alikhanov, A. I. Babaev, M. Ya. Balats, V. S. Kaftanov, L. G. Landsberg, V. A. Lyubimov, Yu. V. Obukhov, Proceedings of the CERN Conference, p. 423 (1962).

M. Banner, J. W. Cronin, J. K. Liu, J. E. Pilcher, Phys. Rev. Letters 21, 1103 (1968).

Particle Data Group, UCRL-8030 (January 1969).

A. Wehmann, F. Engels, Jr., C. M. Hoffmann, P. G. Innocenti, R. Wilson, W. A. Blanpied, D. J. Drickey, L. N. Hand and D. G. Stairs, Phys. Rev. Letters 20, 748 (1968).

11. F. A. Kirsten, UCID-3285 (1968); F. A. Kirsten, UCID-3323 (1969); F. A. Kirsten and D. A. Mack, UCRL-18166 (1968).

12. V. Perez-Mendez, UCRL-17121 (1966).

13. C. C. Lo, UCID-3327 (1969).

14. F. A. Kirsten, UCID-3133 (1967).

15. J. D. Kuehler and H. R. Kerby, Proceedings Fall Joint Computer Comference 1966.

TABLE II

K_L^o Decay Mode	p^*(MeV/c)	Branching Ratio Relative to All Decay Modes
e^+e^-	249	-
$\mu^\pm e^\mp$	238	-
$\mu^+\mu^-$	225	-
$\pi^+\pi^-$	206	0.157%
$e^\pm\pi^\mp\nu$	$\leq$229	38%
$\mu^\pm\pi^\mp\nu$	$\leq$216	28%
$\pi^+\pi^-\pi^o$	$\leq$133	13%

FIGURE CAPTIONS

Fig. 1 Schematic of angular trigger requirement. A secondary trajectory with transverse momentum p^* is bent parallel to the parent independent of the parent momentum.

Fig. 2 Definition of θ^*. $\hat{p}_K$ is a unit vector in the direction of the kaon's laboratory momentum.

Fig. 3 Schematic of the double-armed spectrometer system. The chronotrons were fast counter systems used to improve time resolution.

Fig. 4 $K\mu 3$ neutrino energy spectrum. Only events with the neutrino energy less than a few MeV were accepted by the trigger.

Fig. 5 Detection efficiency of the six rear hodoscope in coincidence with one of the front hodoscope staves for the two-body decay modes. The column output numbers correspond to the six staves in coincidence. This is for the magnet line integral set for the transverse momentum of the $K\mu\mu$ mode.

Fig. 6 Schematic of the matrix unit coincidence wiring. The hodoscope counters were numbered outward from the beam. The front and rear hodoscopes on one side of the spectrometer were fed into the left and right sides of the matrix unit. If two signals met at a coincidence chip, here represented by a dot, a pulse would be sent down the output column.

Fig. 7 Chronotron scintillator system. Pulses from the top or bottom of the scintillator meet at the same time, although at a different place on the diode wheel, independent of the elevation the trajectory through the scintillator.

Fig. 8 Line drawing of one of the picture frame magnets.

Fig. 9 Schematic showing orientation of wands and wires in a spark chamber. The two inner planes of wires were separated by 2 mils of mylar and the high voltage pulse was applied where the buses overlap. The ground wire planes were separated 3/8" from the H.V. planes.

Fig. 10 Schematic of the particle identification devices showing their orientation with respect to the spark chamber trigger scintillator. The detail shows the method used to attach the (Amperex 56 DVP) photomultipliers to the range box scintillators.

Fig. 11 On-line PDP-9 display of an event.

Fig. 12a Plan view of the collimation system.

Fig. 12b Elevation view of the collimation system.

Fig. 13 Distance between left and right trajectories at their intersection in the x-z plane for all two-body candidates.

Fig. 14a Distance of closest approach to target for projected parent particles. All two-body candidates are included.

Fig. 14b Distance of closest approach to target for projected parent particle. Only events with both secondaries stopping before the range box are included.

Fig. 15a Invariant mass of all events with parents appearing to come from less than 2" away from the target and having an invariant mass within 20 MeV of the kaon mass when interpreted as $K_{\pi\pi}$. The background is mostly from $K_{\mu 3}$ events.

Fig. 15b Same as 15a but restricted to those events with both secondaries stopping before the range boxes.

Fig. 16a Invariant mass of $K\pi\pi$ candidates taken with the magnets set for the transverse momentum of the $K\mu\mu$ mode. The dashed line represents the eyeball background subtraction which was made.

Fig. 16b Same as 16a but with all $K\pi\pi$ candidates from runs with magnets set for the transverse momentum of the $K\pi\pi$ mode.

Fig. 17 Final two–lepton candidates after requiring that muons penetrate the range box to within 3 cells of their expected range. There were no K_{ee} candidates.

Fig. 18 Orbit characteristics for the two $K\mu\mu$ candidates with invariant mass greater than 486 MeV. Orbits for trajectories from the $K\pi\pi$ sample with similar characteristics are compared with the $K\mu\mu$ candidate trajectories with short range. The abscissa is the difference between the actual magnet mid–plane spot measured with the rear spark chambers and the predicted spot based on orbiting the incident trajectory through the measured magnetic field.

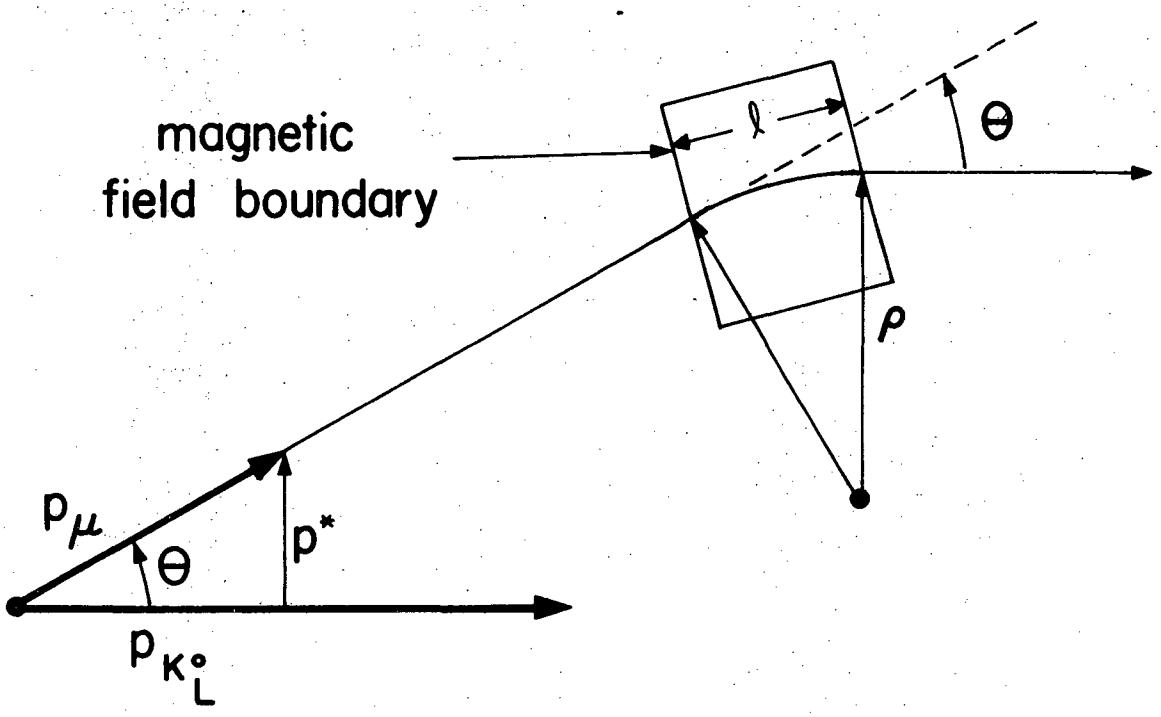

XBL 702-429

fig. 1

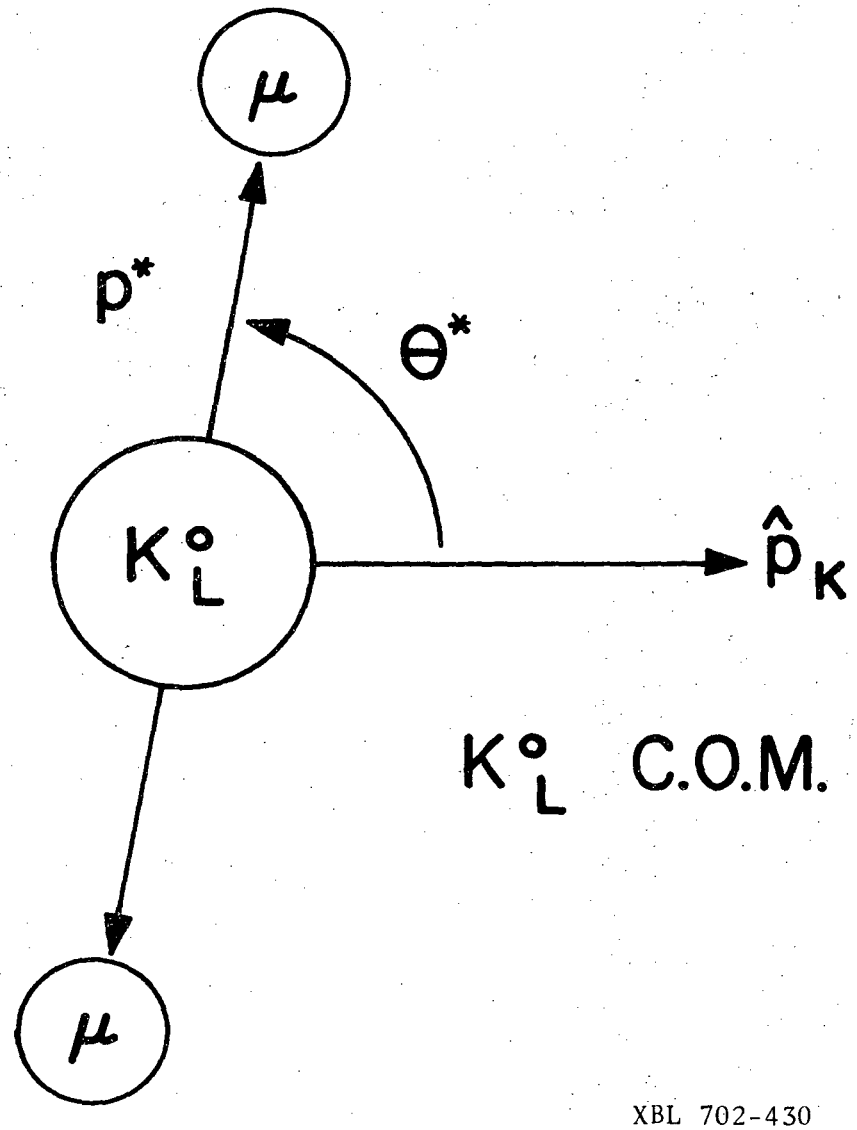

XBL 702-430

fig. 2

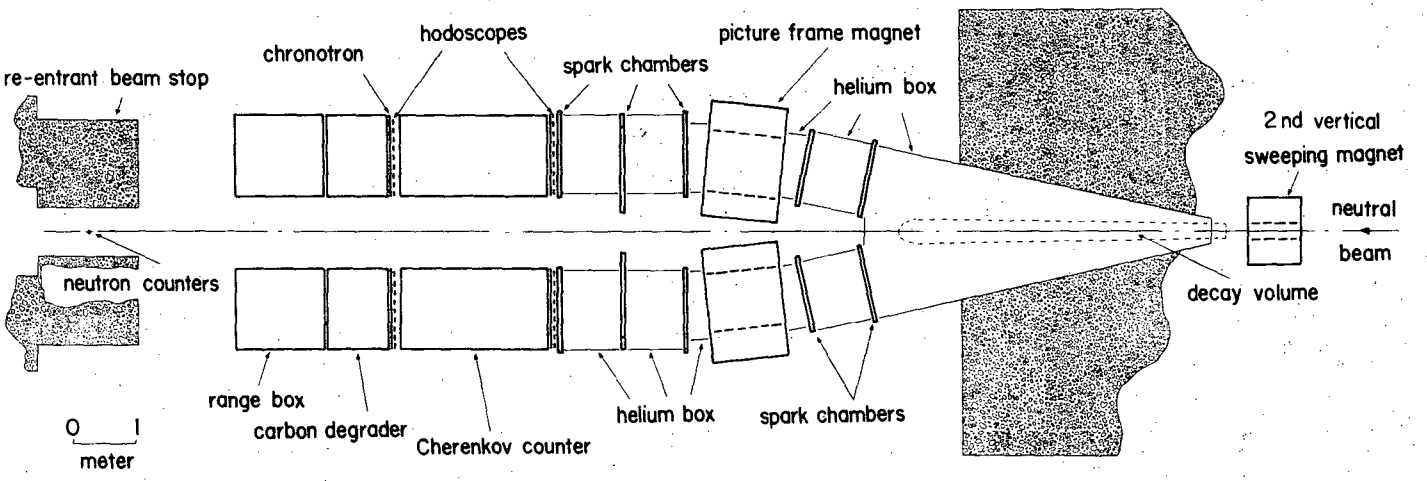
re-entrant beam stop
chronotron
hodoscopes
spark chambers
picture frame magnet
helium box
2nd vertical
sweeping magnet
neutral
beam
neutron counters
decay volume
range box
carbon degrader
Cherenkov counter
helium box
spark chambers
0 1
meter
XBL 702-315

Fig. 3

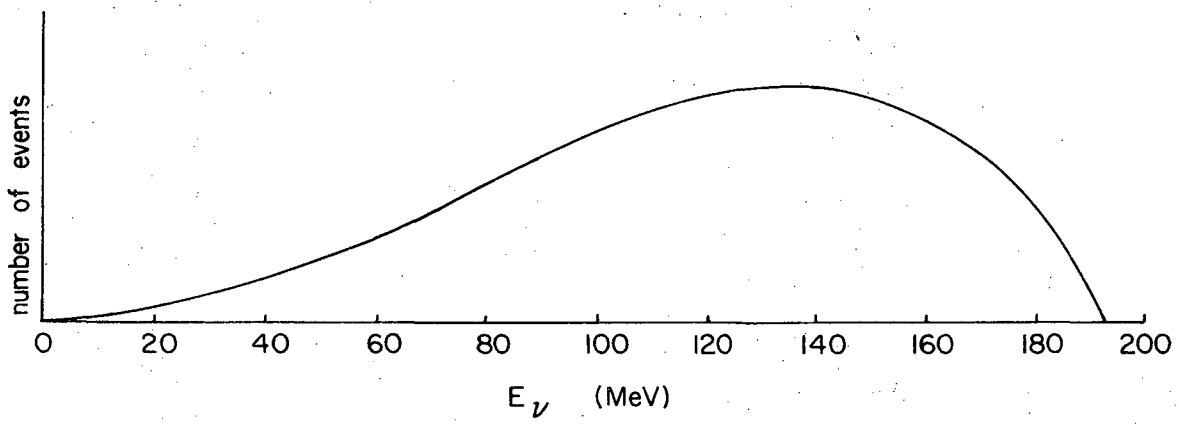

XBL 702-428

fig. 4

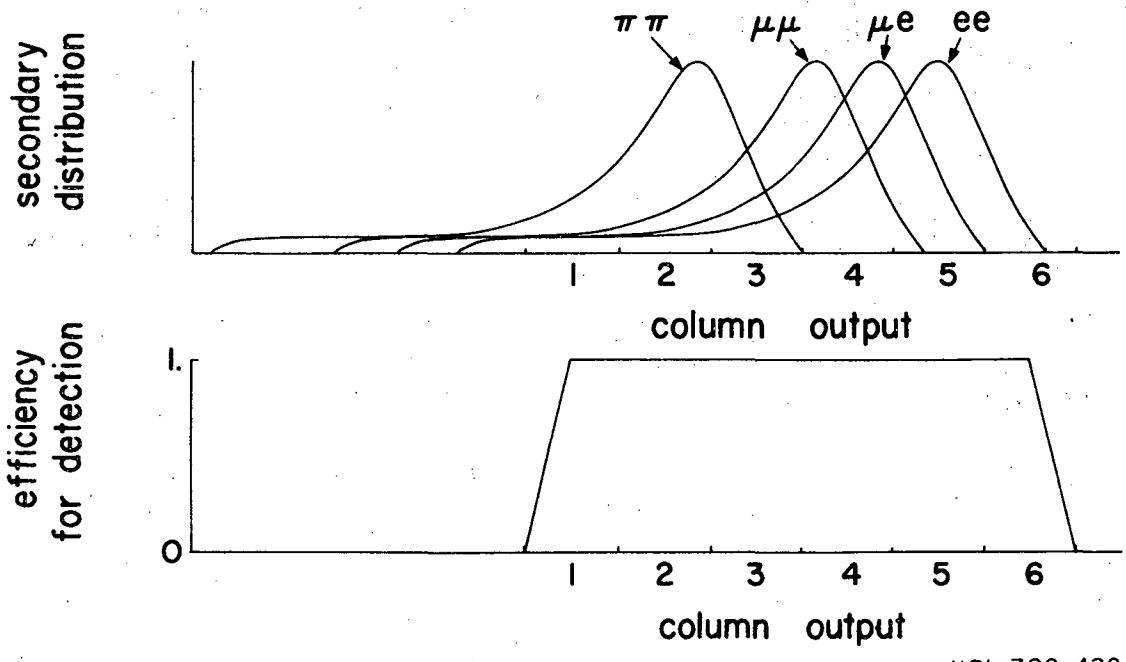

XBL 702-432

fig. 5

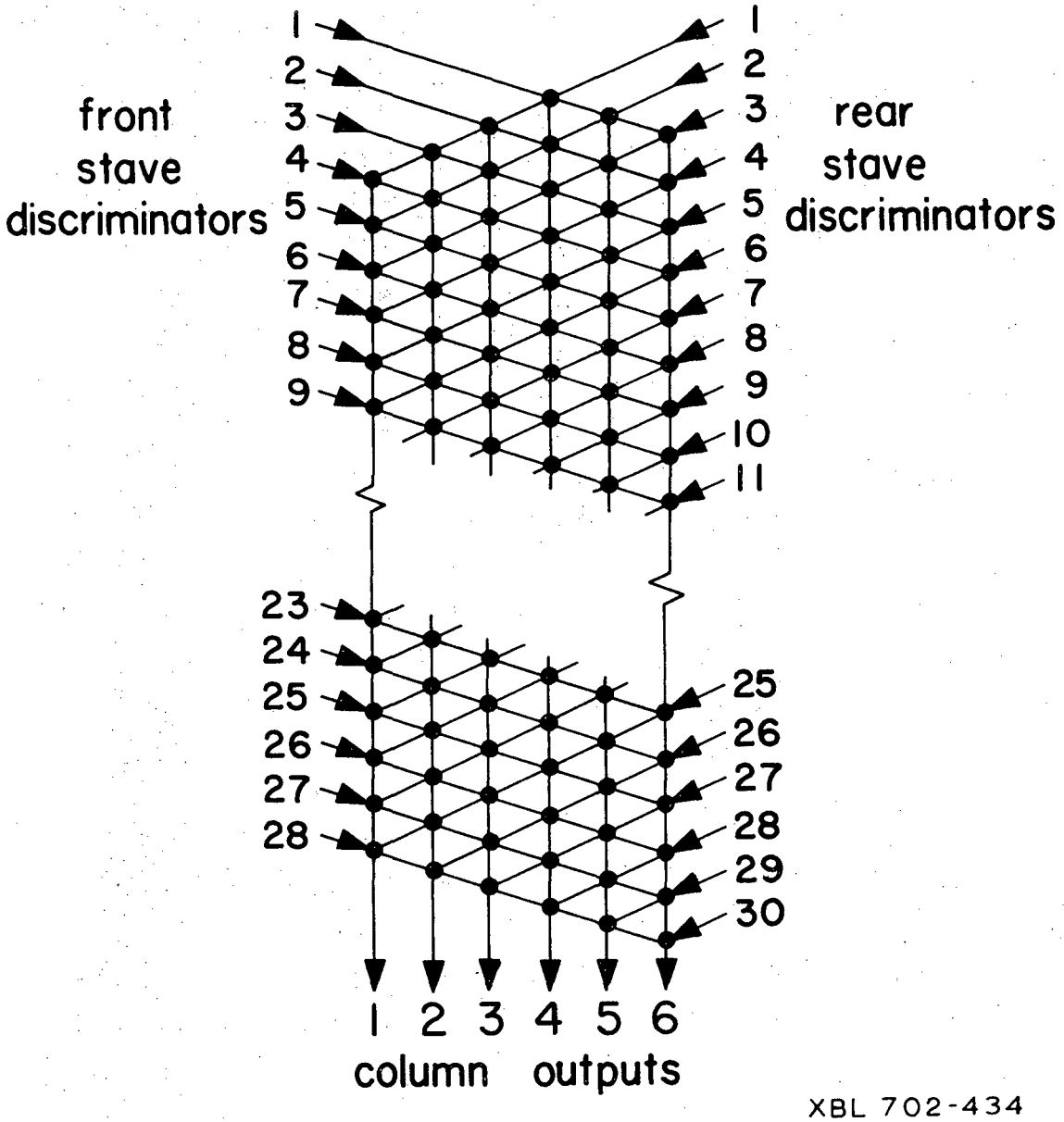
front
stave
discriminators
rear
stave
discriminators
1
2
3
4
5
6
7
8
9
10
11
23
24
25
26
27
28
29
30
1 2 3 4 5 6
column outputs
XBL 702-434

Fig. 6

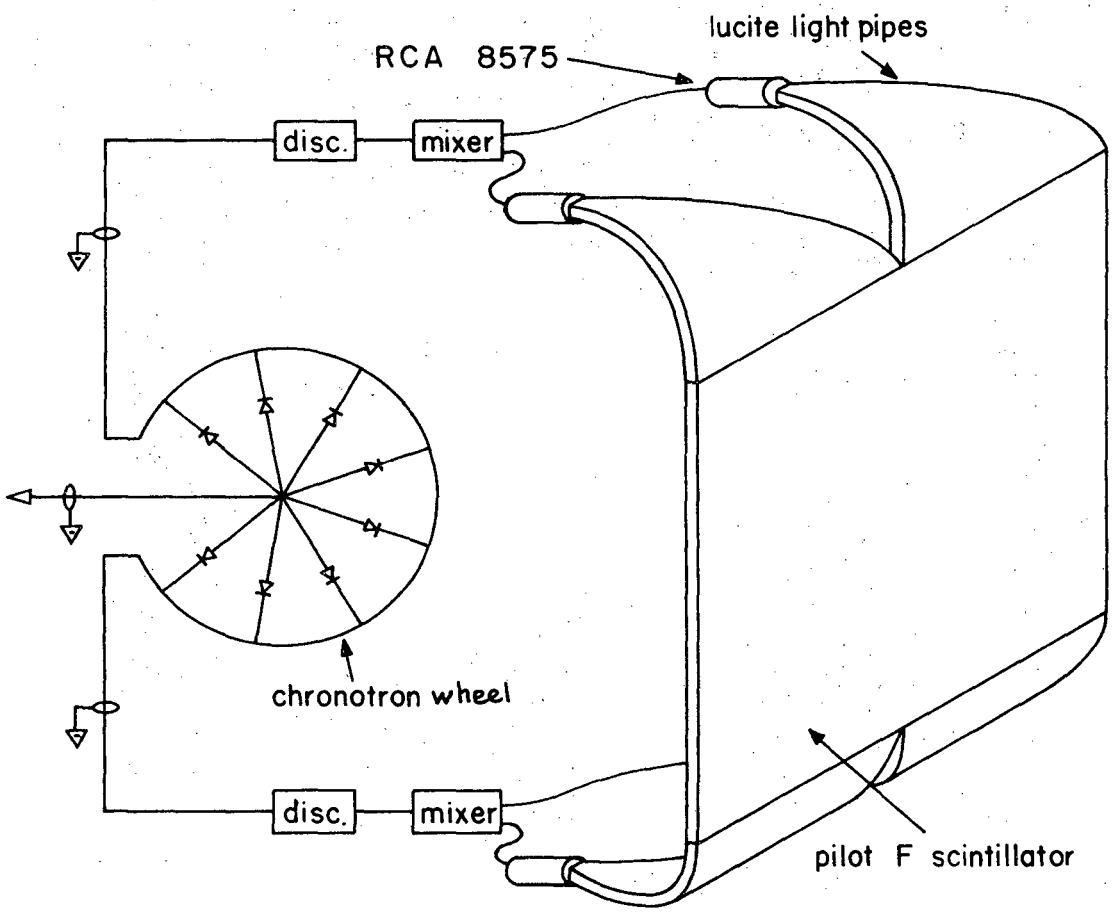
lucite light pipes
RCA 8575
disc.
mixer
chronotron wheel
disc.
mixer
pilot F scintillator
XBL 702-433

fig. 7

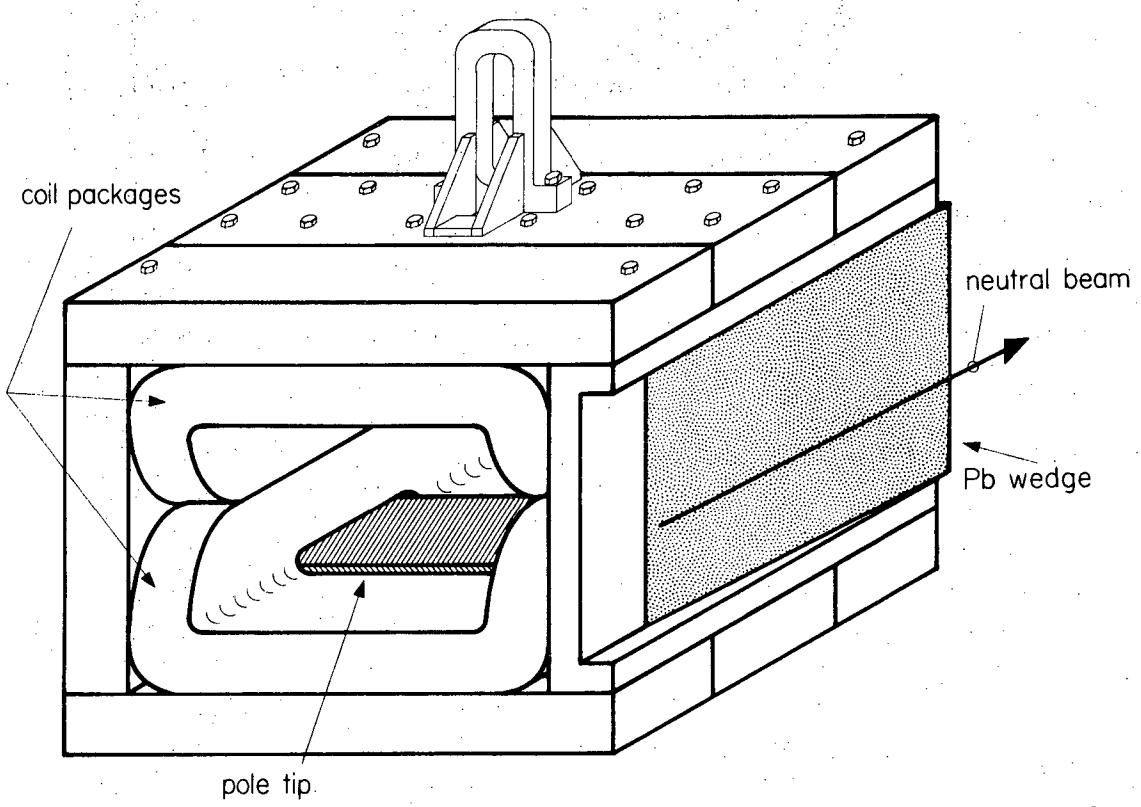

Fig. 8

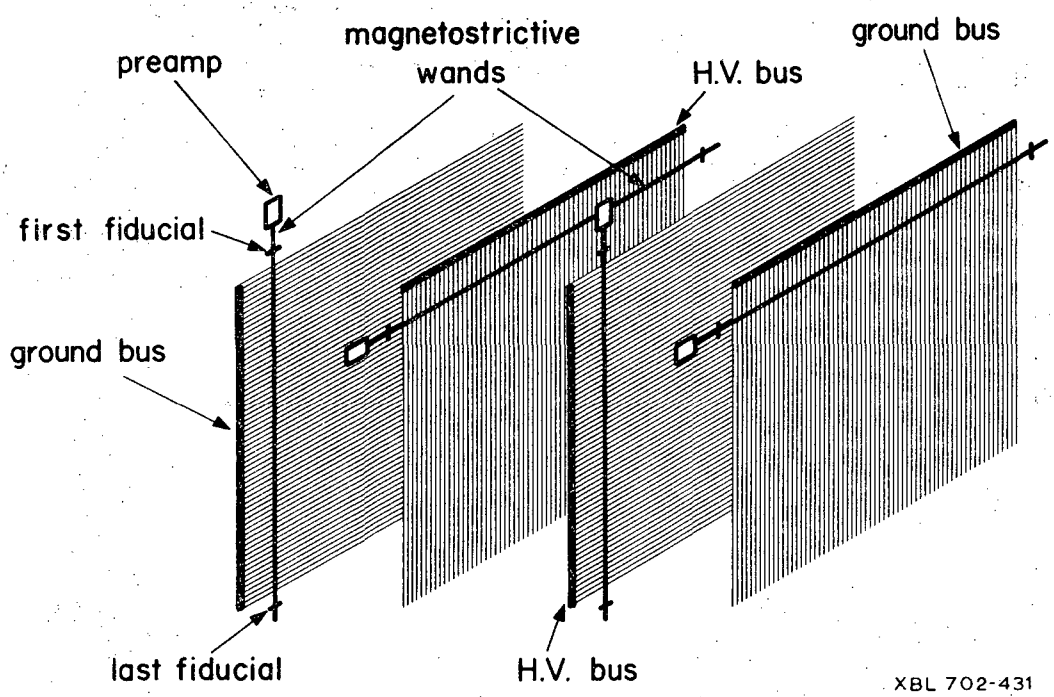
preamp
magnetostrictive wands
H.V. bus
ground bus
first fiducial
ground bus
last fiducial
H.V. bus
XBL 702-431

Fig. 9

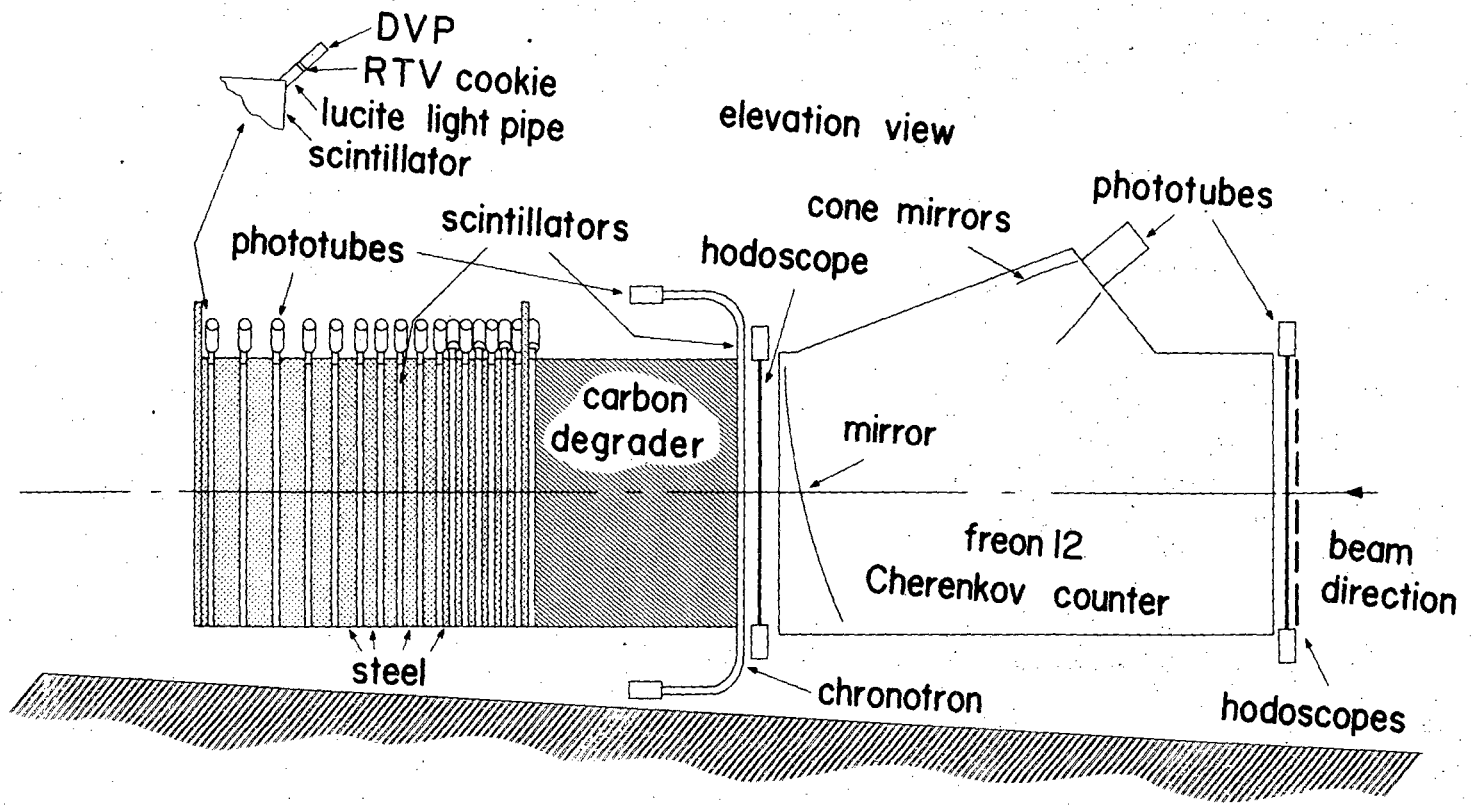

XBL 702-316

Fig. 10

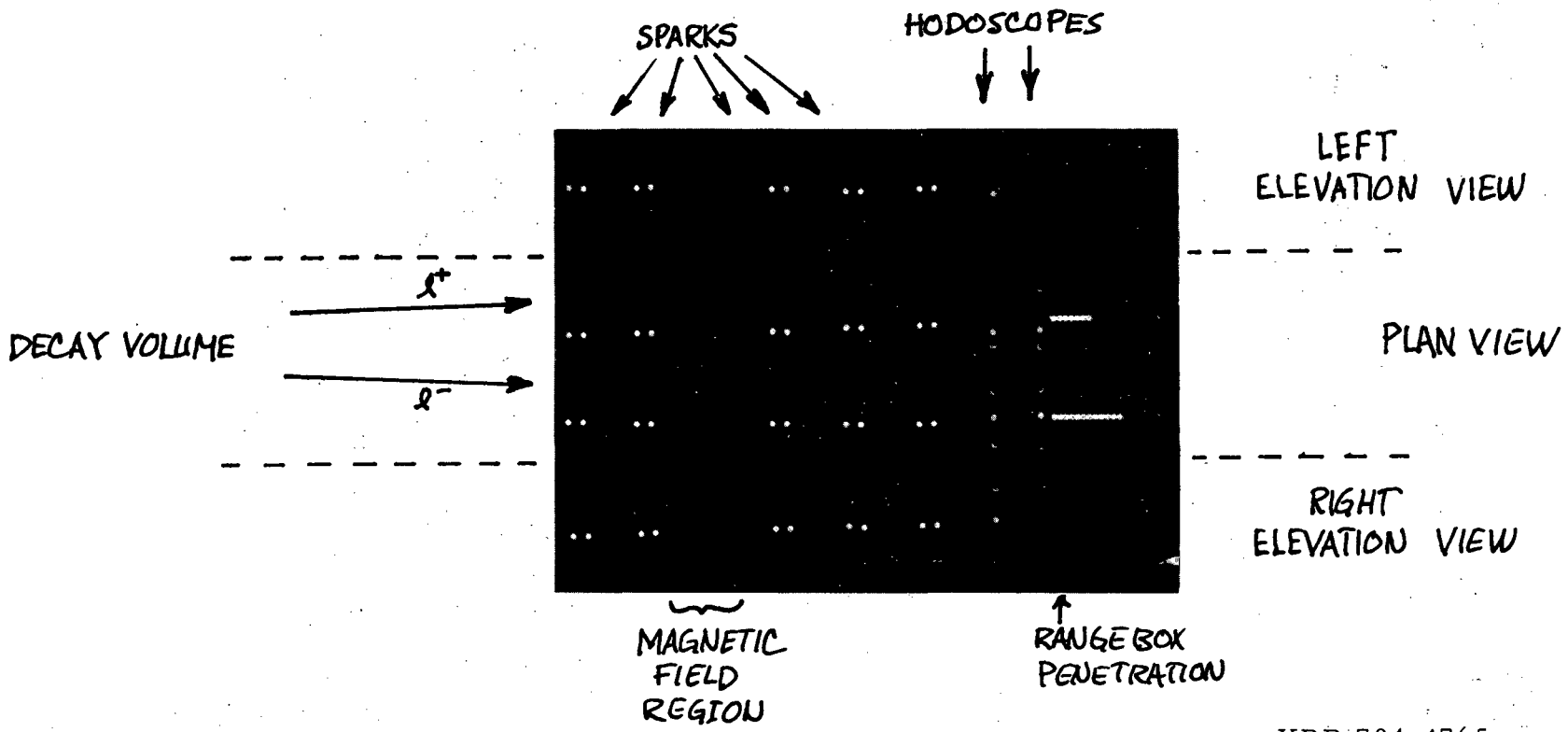
SPARKS
HODOSCOPES
LEFT
ELEVATION VIEW
DECAY VOLUME
PLAN VIEW
RIGHT
ELEVATION VIEW
MAGNETIC
FIELD
REGION
RANGE BOX
PENETRATION
XBB 704-1765

Fig. 11

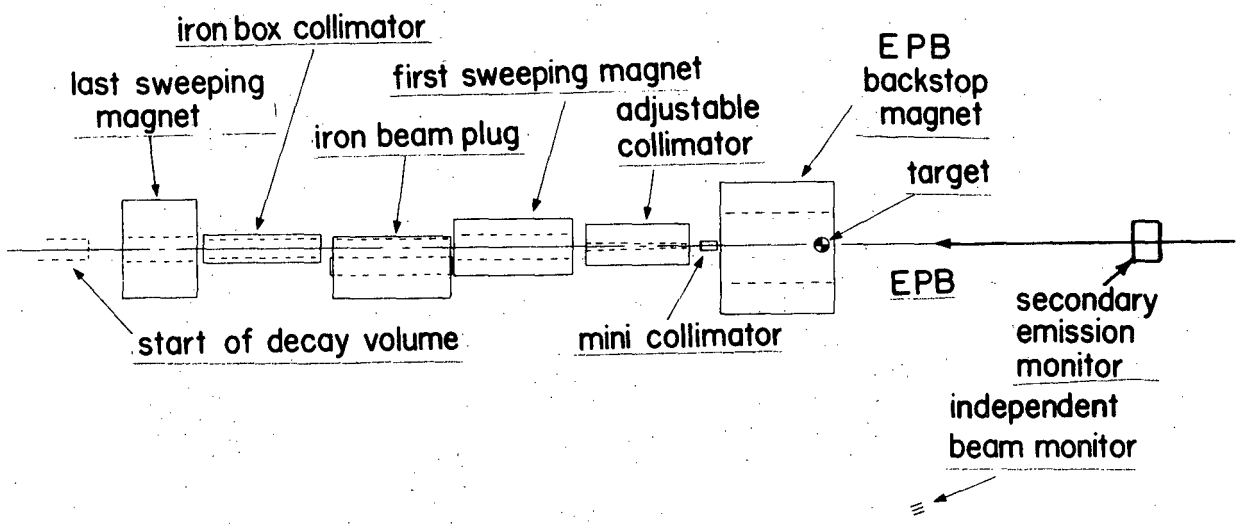

fig. 12a

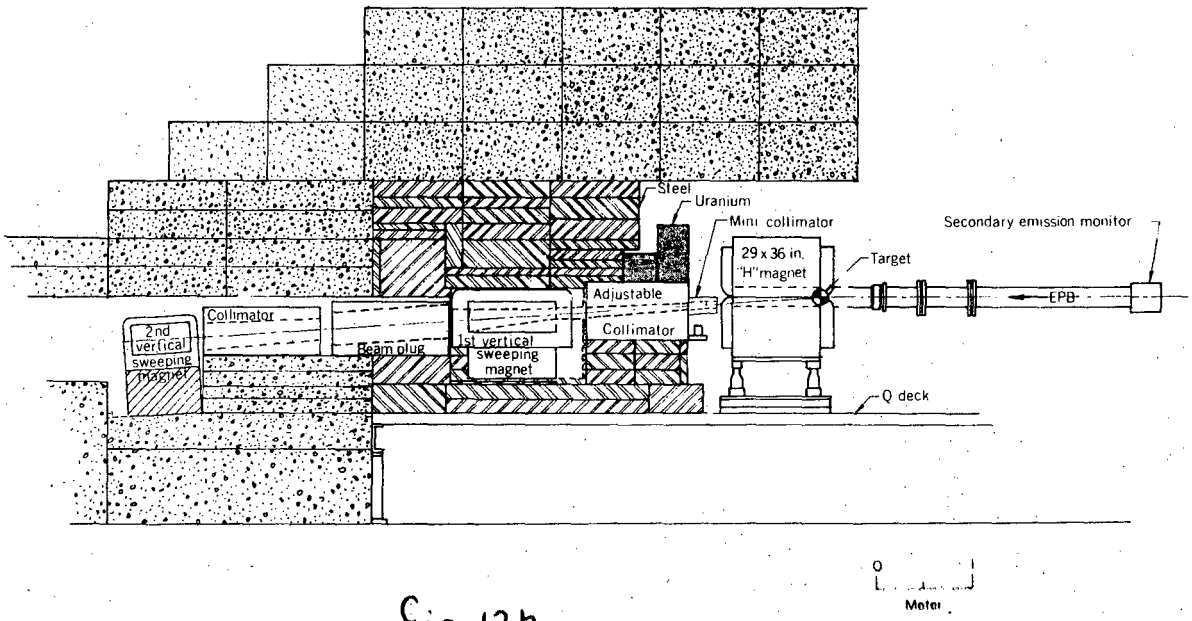

fig. 12b

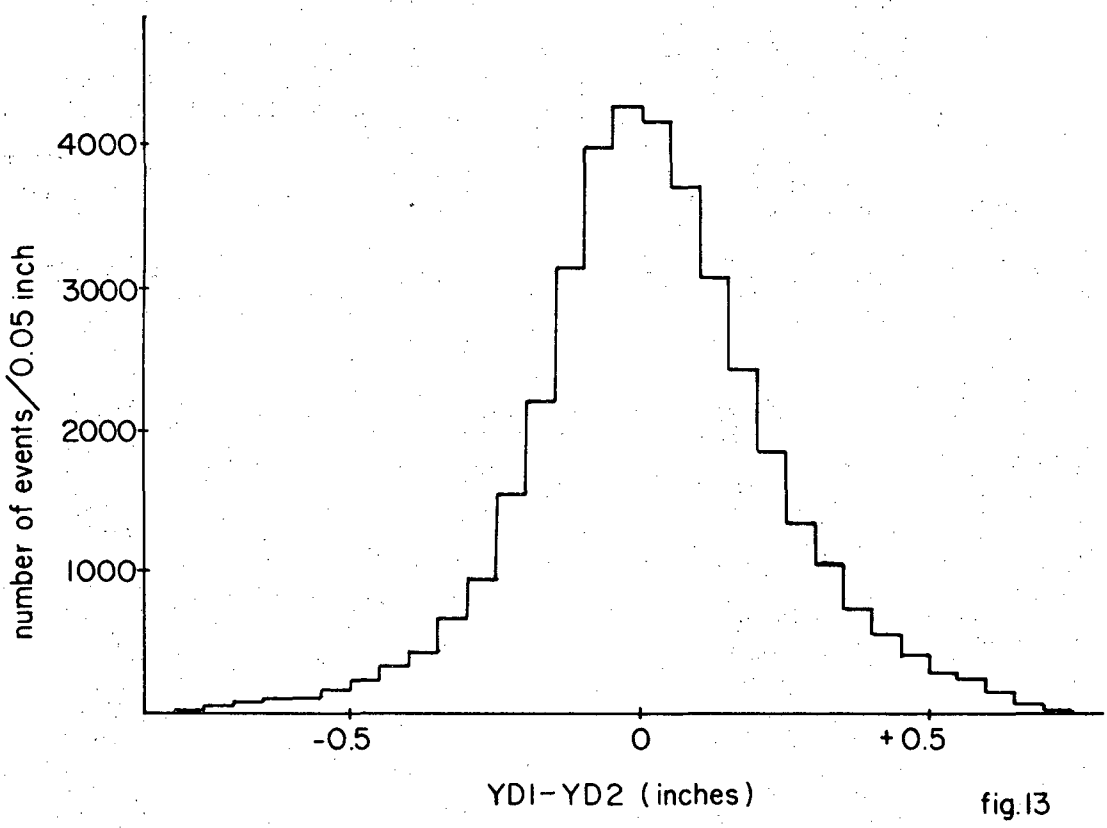

fig.13

XBL 703-615

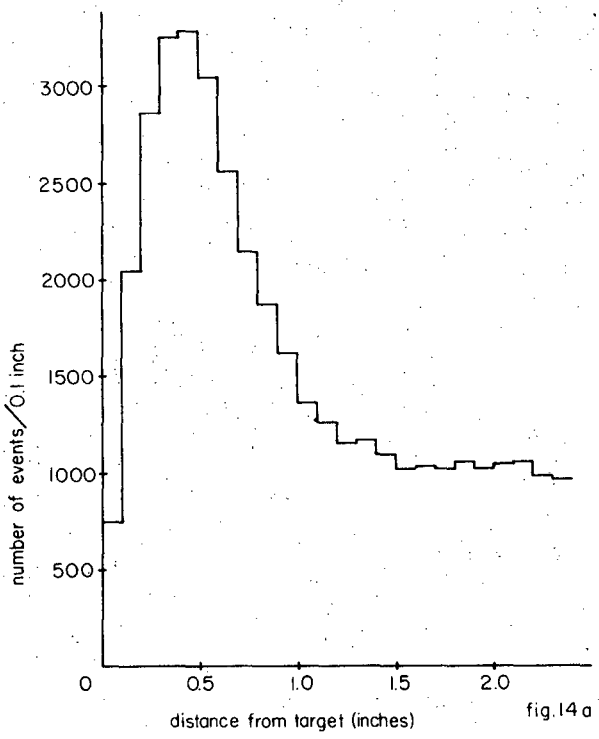

fig. 14 a

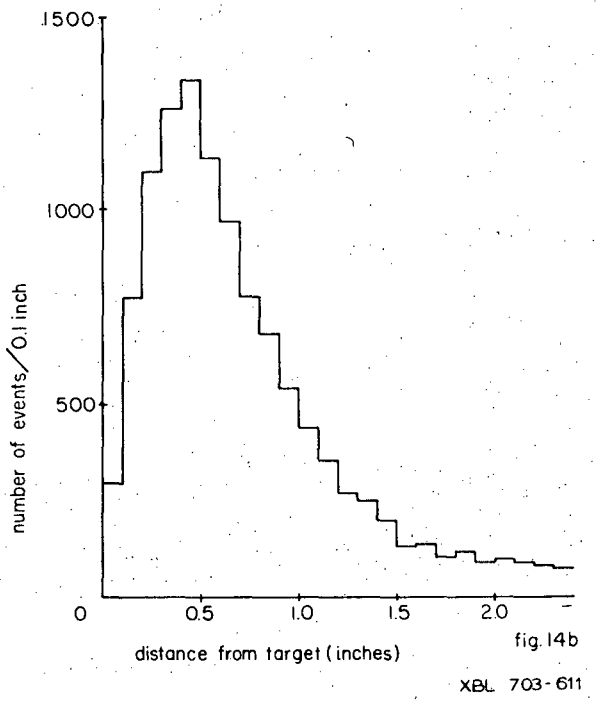

fig. 14 b

XBL 703-611

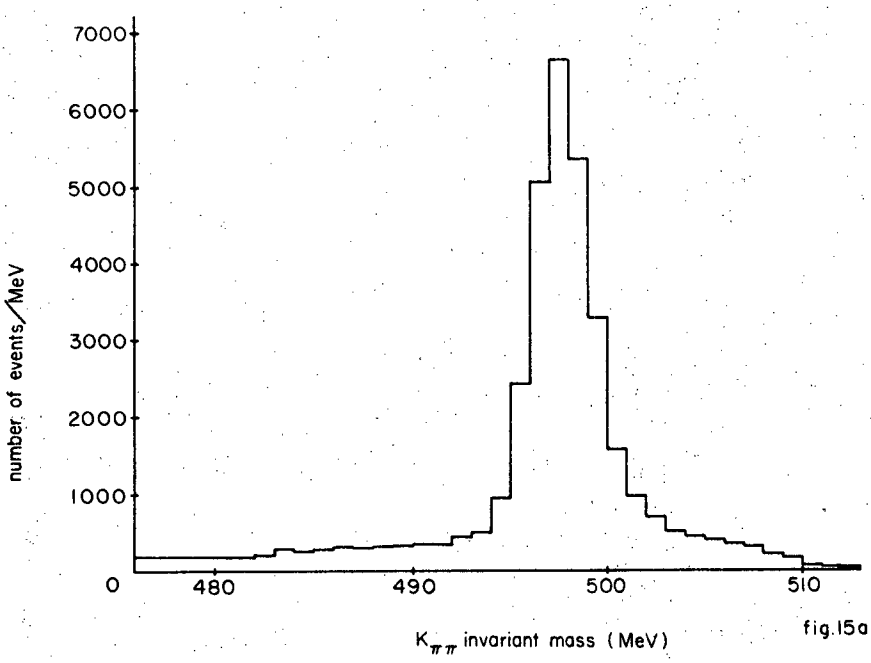

fig.15a

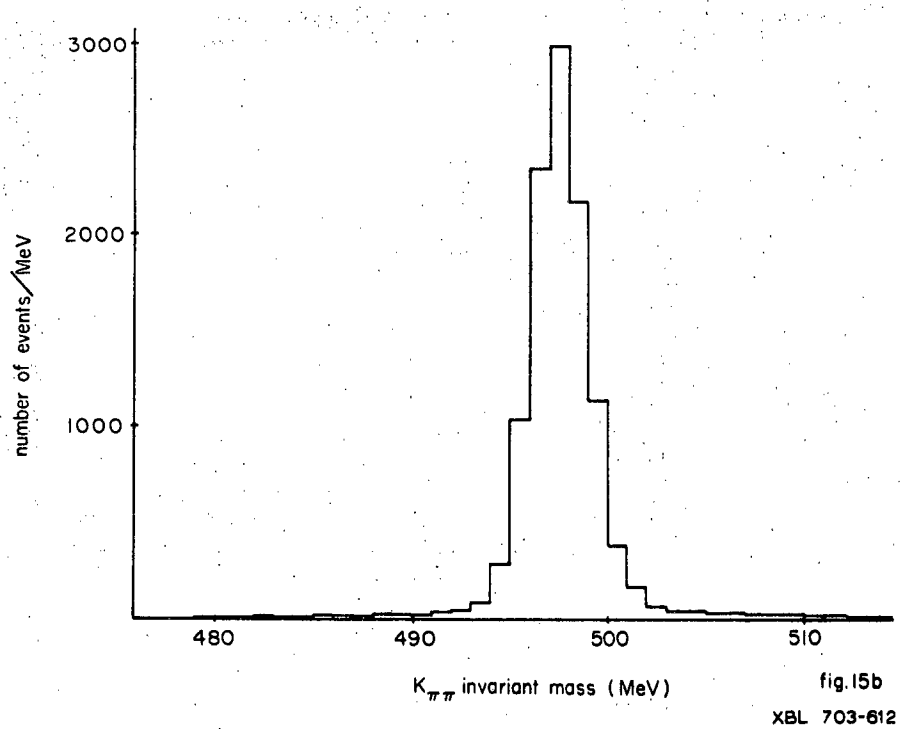

fig.15b

XBL 703-612

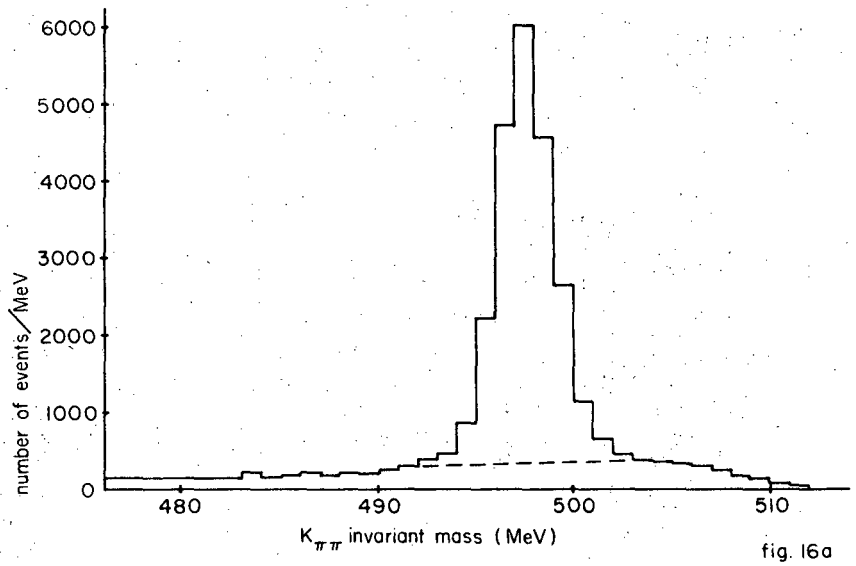

fig. 16a

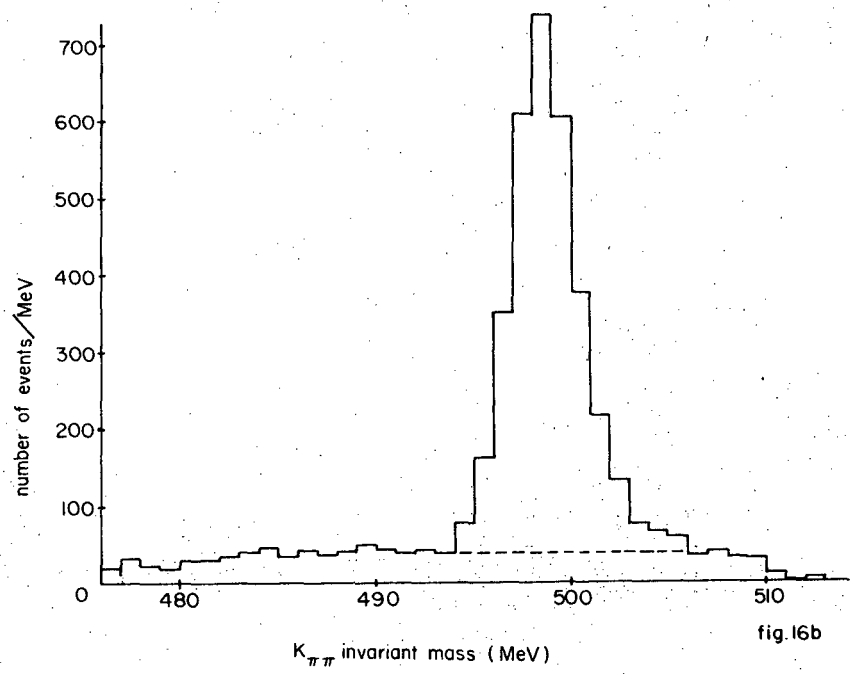

fig. 16b

XBL 703-613

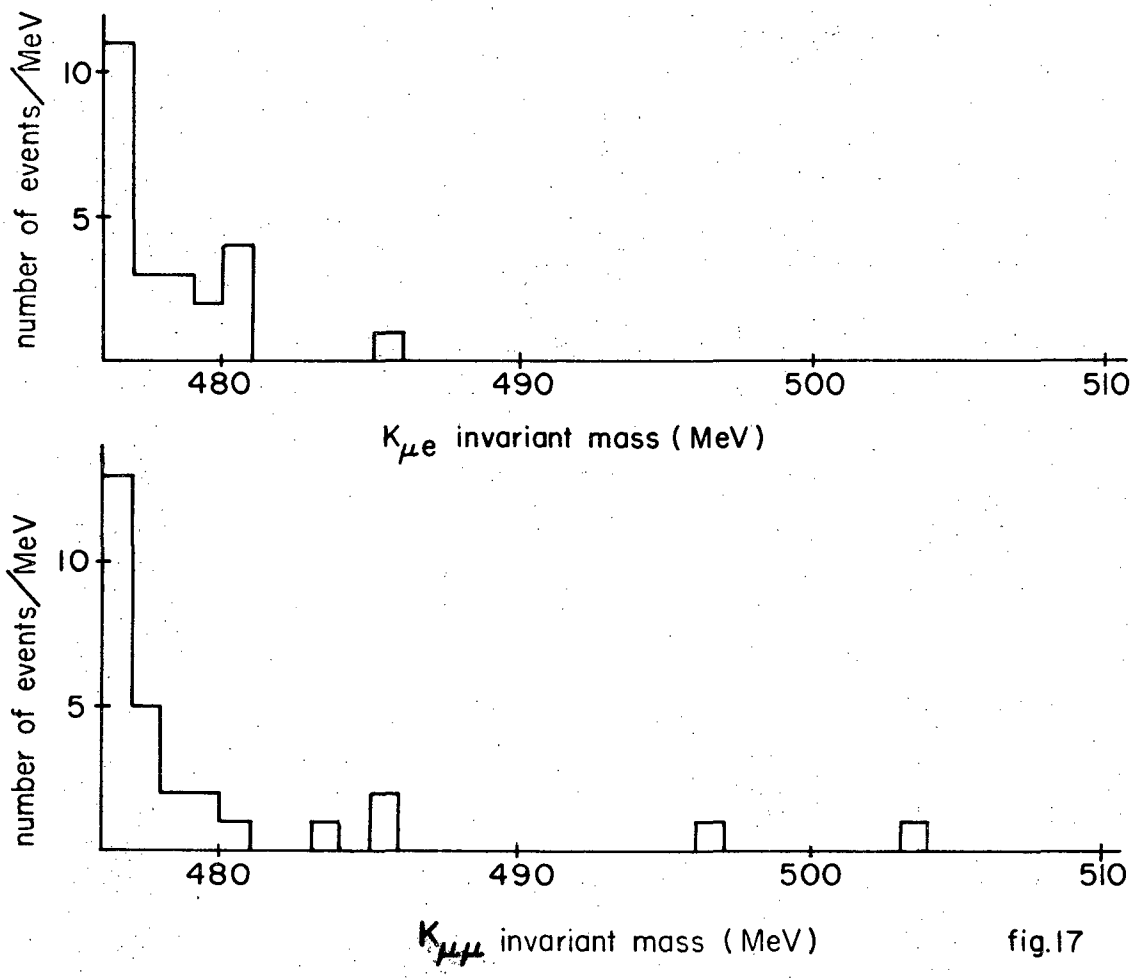

fig.17

XBL 703-614

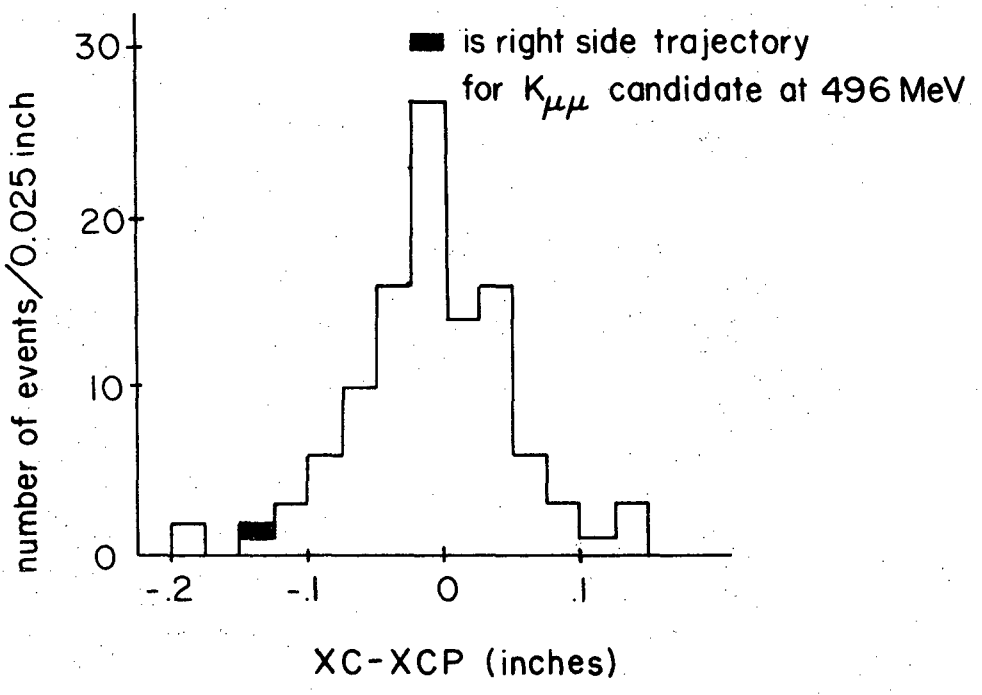

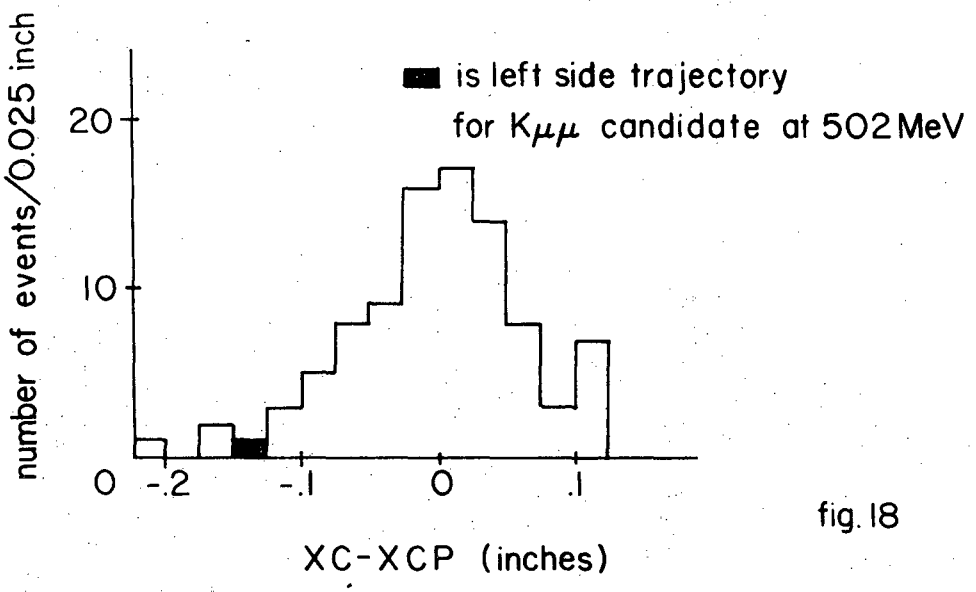

fig. 18

XBL 703-616

LEGAL NOTICE

This report was prepared as an account of Government sponsored work. Neither the United States, nor the Commission, nor any person acting on behalf of the Commission:

A. Makes any warranty or representation, expressed or implied, with respect to the accuracy, completeness, or usefulness of the information contained in this report, or that the use of any information, apparatus, method, or process disclosed in this report may not infringe privately owned rights; or

B. Assumes any liabilities with respect to the use of, or for damages resulting from the use of any information, apparatus, method, or process disclosed in this report.

As used in the above, "person acting on behalf of the Commission" includes any employee or contractor of the Commission, or employee of such contractor, to the extent that such employee or contractor of the Commission, or employee of such contractor prepares, disseminates, or provides access to, any information pursuant to his employment or contract with the Commission, or his employment with such contractor.

TECHNICAL INFORMATION DIVISION
LAWRENCE RADIATION LABORATORY
UNIVERSITY OF CALIFORNIA
BERKELEY, CALIFORNIA 94720